Powder Technology 364 (2020) 429–456

Contents lists available at ScienceDirect

Powder Technology

journal homepage: www.elsevier.com/locate/powtec

On the validity of the two-fluid-KTGF approach for dense gravity-driven granular flows as implemented in ANSYS Fluent R17.2

Alexander Busch [a,*], Stein Tore Johansen [a,b]

[a] Norwegian University of Science and Technology (NTNU), Trondheim, Norway
[b] SINTEF Industry, Trondheim, Norway

ARTICLE INFO

Article history:
Received 25 June 2019
Received in revised form 4 January 2020
Accepted 15 January 2020
Available online 22 January 2020

Keywords:
Cliff collapse
Two fluid model
KTGF
Frictional
CFD

ABSTRACT

As a subproblem of solid transport in wellbores, we have investigated the cliff collapse problem by means of the Two-Fluid-Model (TFM), where the rheological description of the second phase (sand) is governed by the Kinetic Theory of Granular Flows (KTGF) and additional closures from soil mechanics for dense (frictional) regions of the solid phase. Using ANSYS Fluent R17.2, we have studied the influence of the aspect ratio and scale of the initial cliff, the scale of the particle size, four different interstitial fluids (air, water, and two viscous but shear-thinning solutions), and the role of the initial condition (IC) of the solid volume fraction. The latter was evaluated by two different strategies: (1) Let solids settle to establish a compacted granular bed in dynamic equilibrium prior to allow the cliff to collapse and (2) simply patch the solid volume fraction into the computational domain at $t = 0$.

While most of the simulations produced a final deposit featuring a slope, validation with experimentally obtained scaling laws from the literature was not comprehensively successful. The primary reason identified is that, at steady-state, for which a sloped deposit must exist, a thin layer at the top of the sediment bed remains flowing, yielding a scale-dependent disintegration of the cliff over longer periods of time which ultimately results in a flat bed. We suspect this phenomenon, hereafter termed *top bed velocity defect*, to be a consequence of the numerical solutions strategy of Fluent which may result in some momentum solid flux imbalance at top-bed regions where the gradient of the solids kinetic/collisional pressure is high.

Comprehensive model tuning is required to yield a better physical representation of the IC. In addition, alternative closures for both solid frictional pressure and solid viscosity may be helpful to better replicate the experimental data. On the other hand, experimental spread and missing experimental data for the shear-thinning fluids requires more comprehensive experimental data for validation purposes.

If the model in its current form is used for transport modeling of cuttings in wellbore flows, the velocity defect will lead to an unknown overestimation of the mass flux of solids. When it comes to the modeling of dune migration, the *top bed velocity defect* will likely cause disintegration of the dune over longer periods of time.

1. Introduction

Granular cliff collapse, i.e. the disintegration of a pile of granular material over time because of gravity, is an often-researched problem because it represents the physics of landslides and it is a comparatively simple problem to study on a laboratory scale. When it comes to modeling, it is the granular flow analog to the dambreak problem in fluid mechanics. Our motivation, however, is slightly different: we are concerned with wellbore flow modeling, where the transported solids may form a bed at the bottom of the annular conduit. Depending on the local inclination of the wellbore and on operational parameters (e.g. fluid throughput, drill pipe rotation, and inclination), ripples and dunes and even avalanches may occur. Due to the scale of the actual wellbore, model validation is often difficult. Hence, we apply our modeling approach, the Two-Fluid-Model (TFM) with closures from the Kinetic Theory of Granular Flows (KTGF) and additional closures from soil mechanics (SM) to handle dense granular regions, to

Abbreviations: 2D-3D, Two-Three dimensional in space; BC, Boundary Condition; CFD, Computational Fluid Dynamics; CCP, Cliff Collapse Problem; DEM, Discrete Element Method; FFR, Free Fall regime; IR, Inertial regime; KTGF, Kinetic Theory of Granular Flows; PAC, Polyanionic Cellulose; RHS, Right Hand Side; SPH, Smooth Particle Hydrodynamics; SM, Soil Mechanics; TFM, Two Fluid Model; VR, Viscous regime.

* Corresponding author.
E-mail addresses: alexander.busch@ntnu.no, alexander.busch@alumni.ntnu.no (A. Busch).

https://doi.org/10.1016/j.powtec.2020.01.043

Nomenclature

Greek symbols

α	Volume fraction
$\dot{\gamma}$	Shear rate, total shear measure
Δ	Difference
η	Apparent shear viscosity
κ	Bulk viscosity
λ	Parameter in Cross material function and cliff collapse scaling law
μ	Newtonian shear viscosity
ϕ	Angle of internal friction
ρ	Density
Θ	Granular temperature

Latin symbols

a	Aspect ratio
c	Coefficient
d	Diameter
$\mathbf{D}$	Rate of deformation tensor
e	Coefficient of restitution
f	Functional
$\mathbf{f}$	Force vector
g	Radial distribution function
$\mathbf{g}$	Gravity
I	Inertial number
$\mathbf{I}$	Identity tensor
k	Granular conductivity
K	Interphase exchange coefficient
n	Parameter in Cross material function and cliff collapse scaling law
p	Pressure
r	Square root of the fluid-solid density ratio
Re	Reynolds number
St	Stokes number
t	Time
T	Relaxation time
$\mathbf{T}$	Stress tensor
$\mathbf{u}$	Phase velocity
V	Volume
w	Width
x, y	Spatial dimension

Indices

0	Zero, initial, $t = 0$, $\dot{\gamma} \to 0$
∞	Infinity, $\dot{\gamma} \to \infty$
c	Collisional
Cr	Cross
D	Drag
f	Fluid (if used as first index), Frictional (if used as second index, e.g. $_{s,f}$)
i, j	Index
k	Kinetic
mpd	Maximum packing density of the model
n	Non-dimensional
p	Particle
s	Solid
T	Transposed

the Cliff Collapse Problem (CCP), which constitutes an extreme case of what might happen in a inclined wellbore in the absence of flow and pipe rotation.

1.1. From cuttings transport modeling to the CCP

When decomposing cuttings transport in wellbores into smaller and simpler cases, one retrieves the classic CCP. Here, a granular column with an initial with x_0, height y_0 and solid volume fraction $\alpha_{s,0}$, as conceptually depicted in Fig. 1, disintegrates under the influence of gravity as soon as one of the side walls, here the Right Hand Side (RHS), is removed.

At *steady-state*, the final shape features the final run-out length x_f, the final deposit height y_f and an inclination angle in the order of the angle of repose of the respective granular material. A review of granular flows in general and dam-break granular flows and the CCP in particular was recently provided by Delannay et al. [1], who pointed out deficiencies of conventional modeling approaches and conclude that only very limited modeling work is available which has actually addressed problems encompassing flows in which dense and dilute regions coexist.

1.2. Experimental work

The CCP has been intensively researched throughout the years as it is both a numerical test case as well as a real-world problem (e.g. land slides, avalanches). While various specific scaling laws for x_f and y_f have been suggested in the literature, some depending on the experimental setup and/or interstitial fluid [2–7], a universal trend is a power-law dependence on the aspect ratio $a = y_0/x_0$. Distinct behaviors are found at small and large a, as well as for different interstitial fluids. A generic non-dimensional framework [1] for x_f and y_f is given as

$$x_{n,f} = \lambda_x a^{n_x} \tag{1}$$

and

$$y_{n,f} = \lambda_y a^{n_y - 1} \tag{2}$$

respectively, where the dimensionless x-coordinate is defined as

$$x_n = \frac{x - x_0}{x_0} \tag{3}$$

and the dimensionless y-coordinate is defined as

$$y_n = \frac{y}{y_0} \tag{4}$$

where the index 0 denotes the initial configuration at flow time $t = 0$.

The coefficients λ_i may account for granular material properties and experimental setups [3], and the exponents n_i account for large aspect ratio effects [3], and both may also account for the granular fluid flow regime [2]. In addition, in case of interstitial liquids, λ_i and n_i may also account for the then relevant role of the initial solid volume fraction [2].

Various experimental studies have shown that in case of dry granular media the CCP scales predominantly with the initial aspect ratio [1–3,6,8,9]. For instance, Lube et al. [3][1] determined for[2]

$$\begin{aligned} a < 1.8: &\quad \lambda_x = 1.6 \quad \& \quad n_x = 1 \\ a > 2.8: &\quad \lambda_x = 2.2 \quad \& \quad n_x = \frac{2}{3} \end{aligned} \tag{5}$$

for the scaling law (1) and for

[1] The parameter values of Lube et al. were determined with quartz sand (\rho_p = 2600 kg/m£, d_p = {0.15, 1.5} mm and \alpha_repose = 29.5°. In addition, rice and sugar were used. Concerning the nondimensional run-out length, there was no difference between the different particles. However, the deposit height for the fine quarts sand (d_p = 0.15 mm) is better described with \lambda_y = 1.1.

[2] Note that in the scaling framework of both Lube et al. [3] and Bougouin and Lacaze [2], $y_n = y/x_0$. Hence, to suit the scaling law definition as used in this study, these $y_n(a)$ scaling laws of have to be divided by the aspect ratio a which then yields the coefficients as given in Eqs. (6) and (8)

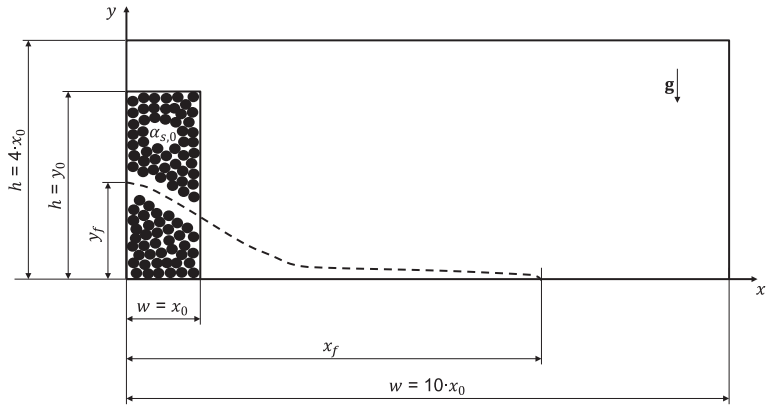

Fig. 1. Conceptual sketch of the CCP with dimensions used in this study. Solid line rectangle filled with particles represents initial condition at $t = 0$, dashed line represent a possible final shape. Large black solid line rectangle represents the dimensions of the computational domain.

$$\begin{aligned} a < 1.15: &\quad \lambda_y = 1 \quad \& \quad n_y = 0 \\ a > 1.15: &\quad \lambda_y = 1 \quad \& \quad n_y = -\frac{2}{5} \end{aligned} \tag{6}$$

for the scaling law (2), in contrast to Bougouin and Lacaze [2],[3] who recently established for the scaling law (1)

$$\begin{aligned} a < 2: &\quad \lambda_x = 2.7 \pm 0.3 \quad \& \quad n_x = 1 \\ a > 2: &\quad \lambda_x = 3.7 \pm 0.3 \quad \& \quad n_x = 0.64 \pm 0.02 \end{aligned} \tag{7}$$

and for the scaling law (2)

$$\begin{aligned} a < 0.75: &\quad \lambda_y = 1 \quad \& \quad n_y = 0 \\ a > 0.75: &\quad \lambda_y = 0.80 \pm 0.07 \quad \& \quad n_y = -0.65 \pm 0.04 \end{aligned} \tag{8}$$

The CCP with an interstitial liquid has been far less investigated. The final run-out length and deposit height does not differ much from the dry case [8]. However, the initial solid volume fraction arises as a relevant parameter [10,11]. Rondon et al. [10] showed that the initial solid volume fraction of the cliff (for instance $\alpha_{s,0} = 0.55$ corresponding to a loose state as a result of plain sedimentation vs. $\alpha_{s,0} = 0.60$ corresponding to a dense state as a result of enforced precompaction) is a major parameter affecting the dynamics of the collapse. The loose configurations collapse rapidly on time scales proportional to the initial heights and result in elongated final deposits with a decreasing slope for decreasing volume fractions. Dense configurations feature much smaller dynamics on time scales that increase with increasing volume fractions. For instance, for initially loose beds ($\alpha_s = 0.55$) of sand collapsing in a fluid, the time to steady-state of the collapsing cliff is in the order of 1 s, whereas for initially dense beds ($\alpha_s = 0.60$), it takes about 30–40 s until the final state is reached [10]. The final slopes of these deposits are approximately constant and equal to the material's angle of repose. A physical explanation is that for the dense cliff to flow the solids need too dilate first, which results in liquid flowing into the cliff due to a negative pore pressure opposing the disintegration. By contrast, the loose column ejects liquid because of positive pore pressure which enhances the disintegration of the cliff.

Recently, Bougouin and Lacaze [2] showed that collapses of a granular column and the corresponding flow regimes may be characterized by a Stokes number in the form of

$$St = \frac{\sqrt{0.5\rho_s \Delta\rho \|\mathbf{g}\| d_s^3}}{18\eta} \tag{9}$$

and the square root of the fluid-solid density ratio

$$r = \sqrt{\frac{\rho_s}{\rho_f}} \tag{10}$$

and may be consequently categorized into one of the following granular flow regimes:

- **Free Fall Regime** (FFR) for $St \gg 1$ and $r \gg 1$, typically the dry case, where the ambient fluid has no effect on the collapse.
- **Inertial Regime** (IR) for $St \gg 1$ and $r \ll 1$, where the individual grain reaches its inertial limit velocity and gravity is balanced by fluid drag force.
- **Viscous Regime** (VR) for $St \ll 1$, where the individual grain reaches its Stokes limit velocity.

Furthermore, Bougouin and Lacaze [2] showed that the coefficients given in Eq. (7) and (8) only apply to the FFR and the IR. The VR features different coefficients instead. The coefficients for the VR run-out length are

$$\begin{aligned} a < 2: &\quad \lambda_x = 1.5 \pm 0.1 \quad \& \quad n_x = 1 \\ a > 2: &\quad \lambda_x = 1.9 \pm 0.1 \quad \& \quad n_x = 0.64 \pm 0.02 \end{aligned} \tag{11}$$

and for the deposit height

$$\begin{aligned} a < 0.75: &\quad \lambda_y = 1 \quad \& \quad n_y = 0 \\ a > 0.75: &\quad \lambda_y = 0.87 \pm 0.03 \quad \& \quad n_y = -0.52 \pm 0.02 \end{aligned} \tag{12}$$

1.3. Modeling work

Two major modeling approaches are typically utilized for the rheological description of the granular matter:

1. Simplifying the granular media to a single phase yet complex fluid, a so-called $\eta(I)$-rheology, where the viscosity coefficient is a function of the inertial number $I = 2\dot{\gamma} d_s / \sqrt{p/\rho_s}$ and goes from a minimum value for low I characterizing the quasi-static regime to an asymptotical finite value for large values of I [1,12–16].
2. Using a Two-Fluid-Model framework and assuming additivity [17], the solid stress tensor is decomposed into two contributions, the first, namely $\mathbf{T}_{s,k/c}$, based on the Kinetic Theory of Granular Flows (KTGF) developed by Savage [18–20] handling the loose, i.e. the collisional/kinetic regime1F[4] ($\alpha_s < \alpha_{s,f}$) and the second, namely $\mathbf{T}_{s,f}$, utilizing closures from soil mechanics describing the dense regime

[3] Bougouin and Lacaze used spherical glass beads with \rho_p = {2500, 2230} and d_p ≈ {1, 3} mm, respectively.

[4] By some researchers referred to as inertial regime or viscous regime.

($\alpha_s > \alpha_{s,f}$)[5], where frictional contacts dominate. Various closure laws exist for the solid pressure $p_{s,k/c}$ [20] and solid viscosity $\eta_{s,\,k/c}$ [20] being mainly a function of the granular temperature θ and the solid volume fraction α_s. Some closures exist for the frictional pressure $p_{s,f}$ [21,22] and frictional viscosity $\eta_{s,f}$ [22,23] being a function of the solid volume fraction α_s and the magnitude of the solid shear rate tensor $\dot{\gamma}_s = \|\dot{\boldsymbol{\gamma}}_s\|$ as well as the solid pressure p_s,.respectively.

The inertial number dependent rheology may be considered much more general than the TFM-KTGF-SM framework. The former accounts for the transition between frictional and collisional regimes in a continuous and physical manner (It can be correlated to physical parameters like particle diameter, inter-particle friction and particle stiffness) while the latter is simply based on a discrete solid volume fraction threshold. Recently, inertial number dependent rheology formulations have been successfully applied to the TFM approach [24,25]. However, such models have not yet found its way into commercial codes.

CFD cuttings transport studies typically employ the second approach. For the sake of completeness, relevant alternative approaches to describe granular flows are Discrete Element Modeling (DEM), e.g. [9,26], where individual particles or parcels are tracked in a Lagrangian manner in addition to the continuum modeling of the carrier phase and Smooth Particle Hydrodynamics (SPH) [27]. DEM methods are however severely limited by affordable and available computational power for larger systems and SPH has not yet gained wide application in industrial environments yet.

The inclusion of the frictional regime is particularly relevant when heap building is of relevance [28]. For instance, when modeling the hour glass problem, heap building in the lower chamber does not occur if the solid stress tensor does not include $\mathbf{T}_f$ with a solid viscosity material function accounting for plasticity [28]. A widely used model is the one of Schaeffer [23], which is based on a Mohr-Coulomb yield criteria and produces large frictional viscosities in case of vanishing shear rates and high solid pressures such that flow is effectively blocked.

For small aspect ratios, the frictional viscosity is dominating the dynamics [29], while for larger aspect ratios, where inertia and velocity magnitudes become much larger, the inclusion of either a $\eta(I)$-description [15] or a KTGF-description [30] appears required to account for the different dynamics.

Savage et al. [31] recently showed that a mixture model approach with the inclusion of the Schaeffer [23] frictional viscosity model is a suitable alternative to model the collapse of granular media for both air and water as interstitial fluid. However, for three-dimensional cuttings transport modeling, the mixture model is not as suited as the TFM because of very heterogeneous solid concentrations.

1.4. Scope and structure

Recent studies [32,33] question the applicability of the classical Schaeffer frictional viscosity model [23] and found that different yield criteria and frictional viscosity closures are required. In contrast, the inclusion of these models is required to properly describe dense granular shearing flows with the KTGF [30].To evaluate the validity of the prescribed modeling approach for cuttings transport problems, where dense sediment beds may form at the lower wall of the annular flow domain, we investigate the cliff collapse problem for granular media (sand in air, water and two shear-thinning aqueous polymer solutions) on nine different spatial scales (respective combinations of three domain sizes and three particle diameters) for different initial aspect ratios and solid volume fractions of the cliff.

The important question is whether in the absence of external flow, i.e. the drilling fluid flushing the annulus, the solid phase behaves like a true granular matter under the pure influence of gravity and eventually stops flowing by building a static bed, satisfying a prescribed angle of repose.

We first provide a description of the physical model, followed by all relevant information on the various cases investigated and the CFD setup and numerical method. We then present all results, where we compare the numerical findings with the aforementioned scaling laws of Lube et al. [3] and Bougouin and Lacaze [2]. In the following discussion, we focus on the observed differences between scaling laws and numerical results as well as the role of the initial solid volume fraction in case of liquid interstitial fluids and the computational procedure utilized.

2. Materials & methods

2.1. Physical model

In the TFM, both the fluid (index f) and the solid (index s) phase are treated as a continuum and assumed both isothermal and incompressible3F[6]. Hence, for an arbitrary volume element V_i, the phase volume fractions α_i must sum to one, i.e.

$$V_i = \int_V \alpha_i dV \quad \wedge \quad \sum_i \alpha_i = 1 \quad \wedge \quad i \in \{f, s\} \tag{13}$$

and mass conservation is given by

$$\frac{\partial}{\partial t}(\alpha_i \rho_i) + \nabla \cdot (\alpha_i \rho_i \mathbf{u}_i) = 0 \tag{14}$$

where the index $i \in \{f,s\}$ and ρ_i and $\mathbf{u}_i$ denote the intrinsic volume averages of density and velocity, respectively.

Both phases obey a general form of the Cauchy momentum transport equation of the form, which for the fluid and solid phase respectively reads

$$\frac{\partial}{\partial t}\left(\alpha_f \rho_f \mathbf{u}_f\right) + \nabla \cdot \left(\alpha_f \rho_f \mathbf{u}_f \mathbf{u}_f\right) = -\alpha_f \nabla p_f + \nabla \cdot (\alpha_f \boldsymbol{\tau}_f) + \alpha_f \rho_f \mathbf{g} - \frac{1}{V}\sum_{p \in V} \mathbf{f}_j \tag{15}$$

$$\frac{\partial}{\partial t}(\alpha_s \rho_s \mathbf{u}_s) + \nabla \cdot (\alpha_s \rho_s \mathbf{u}_s \mathbf{u}_s) = -\alpha_f \nabla p_f - \nabla p_s + \nabla \cdot \boldsymbol{\tau}_s + \alpha_s \rho_s \mathbf{g} + \frac{1}{V}\sum_{p \in V} \mathbf{f}_j \tag{16}$$

where $\boldsymbol{\tau}_i$ is the phasic deviatoric stress tensor comprising some constitutive equation, here a compressible Generalized Newtonian Fluid (GNF) and phase-dependent material functions for the shear and bulk viscosities, η_i and κ_i,

$$\boldsymbol{\tau}_i = 2\eta_i \mathbf{D}_i + \left(\kappa_i - \frac{2}{3}\eta_i\right)(\nabla \cdot \mathbf{u}_i)\mathbf{I} \tag{17}$$

where $\mathbf{D}_i$ is the symmetric part of the fluid or solid velocity gradient (also known as the rate of deformation tensor, or alternatively the rate of strain tensor)

$$\mathbf{D}_i = \frac{1}{2}(\nabla \mathbf{u}_i + \nabla \mathbf{u}_i{}^T) \tag{18}$$

and the shear rate $\dot{\gamma}_i$ is the magnitude of the rate of deformation tensor $\mathbf{D}_i$,

[5] By some researchers referred to as plastic regime or frictional regime.

[6] Note that the solid phase may feature some closure law which accounts for the compressibility of granular matter.

Table 1
Overview of solid phase state equations and material functions used to model the kinetic/collisional (index *k*/*c*) and frictional (index *f*) regimes.

Regime	Quantity	Closure law	Source
Kinetic/collisional ($\boldsymbol{j}=\boldsymbol{k}/\boldsymbol{c}$)	Pressure	$p_{s,k/c}=\alpha_s\rho_s\Theta_s+2\alpha_s{}^2\rho_s\Theta_s\left(1+e_{ss}\right)g_{0,ss}$ (31)	[20]
	Shear viscosity (collisional)	$\eta_{s,c}=\frac{4}{5}\alpha_s{}^2\rho_s d_s g_{0,ss}(1+e_{ss})\left(\frac{\Theta_s}{\pi}\right)^{\frac{1}{2}}$ (32)	[20]
	Shear viscosity (kinetic)	$\eta_{s,k}=\frac{10\rho_s d_s\sqrt{\Theta_s\pi}}{96(1+e_{ss})g_{0,ss}}\left(1+\frac{4}{5}\alpha_s\left(1+e_{ss}\right)g_{0,ss}\right)^{\frac{1}{2}}$ (33)	[34]
	Bulk viscosity	$\kappa_{s,c/k}=\frac{4}{3}\alpha_s{}^2\rho_s d_s g_{0,ss}(1+e_{ss})\left(\frac{\Theta_s}{\pi}\right)^{\frac{1}{2}}$ (34)	[20]
Frictional ($\boldsymbol{j}=\boldsymbol{f}$)	Pressure	$p_{s,f}=0.05\frac{(\alpha_s-\alpha_{s,f})^2}{(\alpha_{s,mpd}-\alpha_s)^5}$ (35)	[21]
	Shear viscosity	$\eta_{s,f}=\frac{p_s\sin\phi_s}{\sqrt{2}\|\mathbf{D}_s\|}$ (36)	[23]
	Bulk viscosity	n/a	n/a

$$\dot{\gamma}_i=\sqrt{2\mathbf{D}_i:\mathbf{D}_i} \tag{19}$$

The closures for the granular viscosities are provided in Section 2.3 and the rheological closure of the fluid is given in Section 2.2.

The last term in Eqs. (15) and (16) represents the momentum transfer of one phase to the other, where the force sum is to be taken over all particles in the volume *V*. We here only consider the drag force $\mathbf{f}_D$, which is typically modeled based on the relative velocity

$$\mathbf{u}_r=\mathbf{u}_s-\mathbf{u}_f \tag{20}$$

as

$$\frac{1}{V}\sum_{p\in V}\mathbf{f}_j=K\mathbf{u}_r \tag{21}$$

where the interphase exchange coefficient *K* is generically expressed as

$$K=\frac{\alpha_s\rho_s f}{T_s} \tag{22}$$

with the Stokes relaxation time T_s written as

$$T_s=\frac{\rho_s d_s{}^2}{18\eta_f} \tag{23}$$

The functional *f* in Eq. (22) includes specific a drag function $c_d(Re_p)$ and depends on the particular model utilized. We use the formulation of Gidaspow [34], which is a combination of the Wen and Yu model [35] and the Ergun equation [36], where the interphase exchange coefficient *K* is given as

$$\begin{aligned}\alpha_s\le 0.2:\quad & K=c_D\frac{3\alpha_s\rho_f\|\mathbf{u}_r\|}{4\alpha_f{}^{0.65}d_s}\\ \alpha_s>0.2:\quad & K=150\frac{\alpha_s{}^2\eta_f}{\alpha_f d_s{}^2}+1.75\frac{\alpha_s\rho_f\|\mathbf{u}_r\|}{d_s}\end{aligned} \tag{24}$$

where the coefficient of drag is defined as

$$c_D=\frac{24}{\alpha_f\,\mathrm{Re}_p}\left(1+0.15(\alpha_f\,\mathrm{Re}_p)^{0.687}\right) \tag{25}$$

and the particle Reynolds number is defined as

$$\mathrm{Re}_p=\frac{\rho_f d_s\|\mathbf{u}_r\|}{\eta_f} \tag{26}$$

2.2. Fluid rheological properties

We here limit the rheological description of a drilling fluid model system to purely shear-thinning behavior. Often, experimental cuttings transport studies utilize polymeric solutions because these are easy to produce, non-hazardous and translucent. The shear viscosity of polymeric solutions is well-characterized by the Cross (Cr) [37] material function

$$\eta_f=\frac{\mu_0-\mu_\infty}{1+\left(\lambda_{Cr}\dot{\gamma}_f\right)^{n_{Cr}}}+\mu_\infty \tag{27}$$

because this represents the shear viscosity data much better for a wider shear rate range since it accounts for Newtonian viscosities at both low and high shear rates [38]. Here, μ_0 is the zero-shear viscosity, μ_∞ is the infinite-shear viscosity, λ_{Cr} is the Cross time constant and n_{Cr} is the Cross exponent. Moreover, this model collapses to the simple Newtonian case for e.g. $\mu_0=\lambda_{Cr}=n_{Cr}=0$.

The fluid phase is assumed incompressible and consequently the bulk viscosity in Eq. (17) becomes zero.

2.3. Solid rheological properties

As mentioned in the introduction, the KTGF framework developed by Savage [18–20] is used to describe the loose, i.e. the collisional/kinetic regime4F[7] (solid volume fraction $\alpha_s<\alpha_{s,f}=0.55$) and additionally closures from soil mechanics are applied to describe the dense regime ($\alpha_s\ge\alpha_{s,f}$) of the solids.

Assuming additivity [17], the entire solid stress tensor, namely Eq. (17) with index *s* and including the solid pressure p_s, is then given by the sum of collisional/kinetic and frictional components

$$\begin{aligned}\mathbf{T}_s&=\mathbf{T}_{s,k/c}+\mathbf{T}_{s,f}\\&=\sum_{j\in\{k/c,f\}}\left[\left(-p_{s,j}+\left(\kappa_{s,j}-\frac{2}{3}\eta_{s,j}\right)\nabla\cdot\mathbf{u}_s\right)\mathbf{I}+2\eta_{s,j}\mathbf{D}_s\right]\end{aligned} \tag{28}$$

Even though the general stencil is that of a compressible Newtonian fluid, namely Eq. (17), the rheological properties of the solid phase given by the respective material functions as summarized in Table 1 are highly non-linear. They depend on a variety of parameters and variables such as the granular temperature Θ_s as a measure for the degree of random particle motion (granular fluctuations due to individual particle collisions), for which the general transport equation reads [39].

[7] In the literature, these regimes are alternatively known as the inertial or viscous regime and the plastic or frictional regime, respectively.

Table 2
Fluid densities and rheological model coefficients at room temperature (21 °C) and atmospheric pressure (1.01 bar).

Fluid	ρ_f [kg/m^3]	Cross model coefficients			
		μ_0 [Pa·s]	μ_∞ [Pa·s]	λ_{Cr} [1/s]	n_{Cr} [−]
Air	$1.225\cdot10^{0}$	0	$1.79\cdot10^{-5}$	0	0
H_2O	$9.980\cdot10^{2}$	0	$1.002\cdot10^{-3}$	0	0
PAC2	$1.000\cdot10^{3}$	$7.210\cdot10^{-2}$	$1.002\cdot10^{-3}$	$1.090\cdot10^{-2}$	0.586
PAC4	$1.000\cdot10^{3}$	$2.140\cdot10^{-1}$	$1.002\cdot10^{-3}$	$2.610\cdot10^{-2}$	0.608

$$\frac{3}{2}\left[\frac{\partial}{\partial t}(\alpha_s\rho_s\Theta_s)+\nabla\cdot(\alpha_s\rho_s\mathbf{u}_s\Theta_s)\right]=\mathbf{T}_s:\nabla\mathbf{u}_s+\nabla\cdot(k_{\Theta_s}\nabla\Theta_s)-D_{\Theta_s}+K_{fs} \tag{29}$$

where k_{Θ_s} is the granular conductivity [e.g. 21] and the two final terms in Eq. (29) are the collisional dissipation of energy [20] and the interphase exchange between the particle fluctuations and the fluid phase [34].The granular temperature Θ_s is defined as

$$\Theta_s=\frac{1}{3}\langle u_{s,i}'u_{s,i}'\rangle \tag{30}$$

where $u_{s,i}'$ is the i-th fluctuating component of the solids velocity and the bracket represents an ensemble average of the fluctuating velocities of all particles within a finite volume [39].

Eq. (29) is simplified to an algebraic equation by neglecting the convection and diffusion terms—an often used assumption in dense, slow moving fluidized beds where the local generation and dissipation of granular temperature far outweigh the transport by convection and diffusion.

In Eqs. (31)–(34), e_{ss} is the coefficient of restitution for particle collisions and

$$g_{0,ss}=\left[1-\left(\frac{\alpha_s}{\alpha_{s,\,\max}}\right)^{\frac{1}{3}}\right]^{-1} \tag{37}$$

is the radial distribution function accounting for the probability of particle collisions, which has been used frequently in the history of granular flows [20,40–42] in the form presented in Eq. (37).

2.4. Test matrix

We investigated the influence of the aspect ratio and scale of the initial cliff ($a=y_0/x_0=1,2,3$, and $x_0=0.1,1,10$ m, respectively), the scale of the particle size ($d_s=10^{-4}, 10^{-3}, 10^{-2}$ m), four different interstitial fluids (air, water, and two viscous but shear-thinning polymer solutions, namely Polyanionic Cellulose with concentrations of 2 g/L and 4 g/L, hereafter termed PAC2 and PAC4, respectively, all material data provided in Table 2), and the role of the initial conditions (ICs) such as solid volume fraction $\alpha_{s,\,0}$ and solid pressure fields. Fig. 2 provides the logical relationship of the investigated parameters for the example of $a=3$.

By letting the solids settle and establish a granular bed in a presimulation, smooth fields for $\alpha_{s,\,0}$ (average $\alpha_{s,\,0}\approx0.59$) and p_s as well as other quantities are obtained which allow for a smooth simulation start when the RHS wall of the cliff is being removed instantly. The alternative is to simply patch the respective $\alpha_{s,\,0}$ into the computational domain, which we have also investigated for a $\alpha_{s,\,0}=\{0.55, 0.60\}$, as depicted in Fig. 2.

For each IC, we investigated the role of four different interstitial fluids (see Table 2) and nine different cases. The latter are spatial combinations of the particle diameter range and the initial cliff scale, as provided in Table 3 and depicted in Fig. 2.

In all cases, the solid phase was replicating sand, represented by mono-sized spherical particles with a density $\rho_s=2560$ kg/m^3. In the frictional closures, namely Eqs. (35) and (36), the angle of internal friction ϕ_s was assumed to be 45° in order to yield an angle of repose of the final deposit of approximately 25°…30° [28], the coefficient of restitution for particle collisions e was taken as 0.9, the maximum packing density of the solid phase $\alpha_{s,mpd}$ was defined as 0.63 and the solid volume fraction threshold for the dense regime, where the frictional model activates, was $\alpha_{s,\,f}=0.50$.

2.5. CFD setup & numerics

For the three cliff scales investigated, three structured quadrilateral 2D meshes with an initial grid size $\Delta x=0.002, 0.02, 0.2$ m were generated. In order to precisely track the evolution of the collapsing cliff, adaptive meshing was used throughout the simulations to refine the mesh based on the magnitude of the solid volume fraction gradient $\|\nabla\alpha_s\|$ every fifth timestep. Depending on the fluid type, simulations were run for 4 s (air, $\Delta t=10^{-4}$ s) or 100 s (all liquids, $\Delta t=10^{-3}$ s) to obtain the final solution.

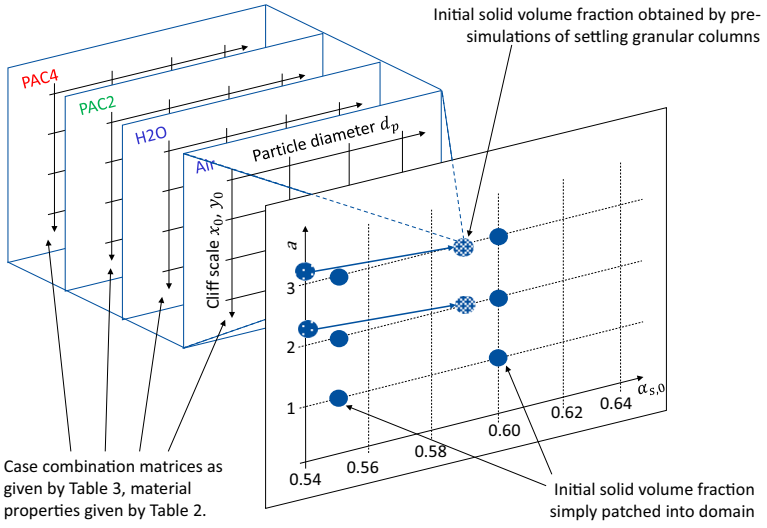

Fig. 2. Different cases investigated. For each combination of aspect ratio a and initial volume fraction $\alpha_{s,\,0}$, the nine spatial combinations provided in Table 3 where simulated for each fluid phase indicated.

Table 3
Investigated combinations of spatial scales for initial cliff and particle. The matrix given by Table 3 is the framework of each of the individual materials for a given aspect ratio as depicted by Fig. 2. The symbols indicated are respectively used in all remaining figures of the paper (unless indicated otherwise).

		Particle scale		
		Small ($\boldsymbol{d_s} = 0.0001$ m)	Medium ($\boldsymbol{d_s} = 0.001$ m)	Large ($\boldsymbol{d_s} = 0.01$ m)
Cliff scale	Small ($\boldsymbol{w} = 0.1$ m, $\boldsymbol{y_0} = 0.04$ m, $\boldsymbol{\Delta x} = 0.002$ m)	1 / ○	2 / ○	3 / ○
	Medium ($\boldsymbol{w} = 1$ m, $\boldsymbol{h} = 0.4$ m, $\boldsymbol{\Delta x} = 0.02$ m)	4 / ◇	5 / ◇	6 / ◇
	Large ($\boldsymbol{w} = 10$ m, $\boldsymbol{h} = 4$ m, $\boldsymbol{\Delta x} = 0.2$ m)	7 / □	8 / □	9 / □

We used ANSYS Fluent R17.2, a commercial Finite Volume code and hereafter simply termed Fluent, to solve the physical model. The flow fields were solved using the Phase-Coupled SIMPLE scheme [43] in a segregated manner (but coupled by phases) with conservative underrelaxation factors, as conceptually shown in Fig. 3.

A shared pressure correction equation is solved, based on total continuity. Fluent is based on a collocated grid and uses a "Rhie and Chow type of scheme to calculate volume fluxes" [45,46]. The solid volume fraction is solved for the secondary phase and the primary phase value is then obtained from the constraint (13). After solving the granular temperature Eq. (29), the solid pressures (31) and (35) are obtained from the solid volume fractions.

The QUICK scheme [44] was applied for spatial discretization and the Green-Gauss node-based gradient scheme to evaluate all gradients. The term ∇p_s in the momentum equation of the granular phase, namely Eq. (15) with index s in combination with Eq. (28), is numerically resolved by $\nabla p_s \approx \partial p_s/\partial \alpha_s \nabla \alpha_s$. The time discretization was implicit second order. The algebraic multigrid method with the Gauss-Seidel solver was used to solve the system of discretized equation.

3. Results

First, we provide a mapping of our investigated cases on the flow regime map of Bougouin and Lacaze [2] because the scaling laws to use for model validation depend on the granular flow regime. Our numerical results are subsequently presented in the following manner: For each of the first phase fluids and initial solid volume fractions investigated, we depict the numerical results in the form of the dimensionless final run-out length and final deposit height per aspect ratio a together with the scaling laws of Lube et al. [3] and Bougouin and Lacaze [2]. Examples of the dimensional final shapes of the deposit, together with the initial shapes and snapshots of the evolution of the cliff disintegration using the matrix framework given in Table 3 and Fig. 2 are provided in Appendix A.

Both the dimensional final run-out length and the dimensional final deposit height were determined based on the maximum of the volume fraction gradient, with restrictions imposed on the y- and x-coordinate, respectively:

$$\begin{aligned} x_f &= x(\max\|\nabla\alpha_s(x, y \geq d_s)\|) \\ y_f &= y(\max\|\nabla\alpha_s(\Delta x, y)\|) \end{aligned} \tag{38}$$

3.1. Granular flow regimes

By expressing our design space in terms of the quantities defining the granular flow regime of Bougouin and Lacaze [2], namely eqs. (9) and (10), we can identify the respective granular flow regimes for the individual cases as depicted on Fig. 4.

The spatial scale of the cliff is not a parameter in the space of Bougouin and Lacaze [2], hence the different spatial scales of the cliff as investigated in this study collapse on one single point, respectively.

The granular flow regime mapping shows that when it comes to the scaling laws of Bougouin and Lacaze [2], the correct scaling benchmark for the air numerical results are given by the coefficients (7) and (8). For the H2O and PAC2 cases, the coefficients (7) and (8) as well as (11) and (12) apply, however, depending on the particle diameter. The PAC4 cases are entirely covered by the coefficients (11) and (12).

3.2. Sand in air

Fig. 5 provides the dimensionless final run-out length and final deposit height for $\alpha_{s,\,0} \approx 0.59$, i.e. where the IC conditions of the

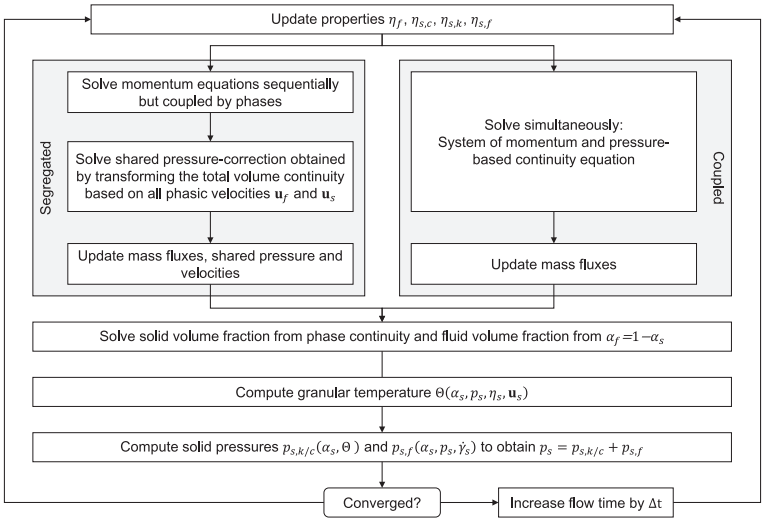

Fig. 3. Computational sequences of ANSYS Fluent R17.2, adapted from [45,46].

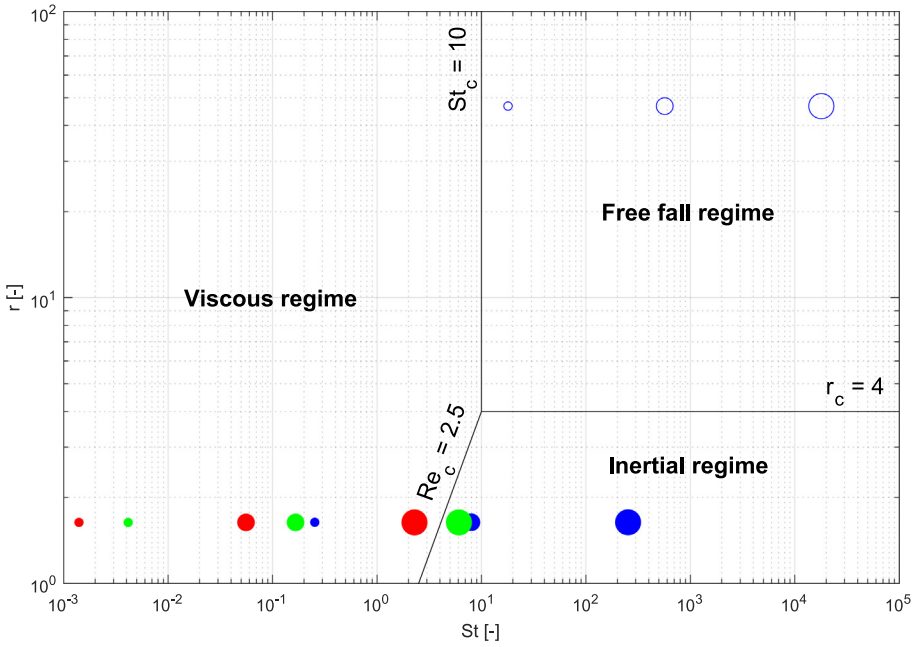

Fig. 4. Different cases investigated mapped on granular fluid flow regime map (square root of grain density ratio r vs. Stokes number St) of Bougouin and Lacaze [2]. Colors indicate fluids as defined in Fig. 2 (blue circled = air, blue filled = H2O) and sizes of data points represent the three different particle diameters. Note that the different symbols as defined in Table 3 fall onto one point because the spatial size of the cliff is not part of the r-St-space of Bougouin and Lacaze [2].

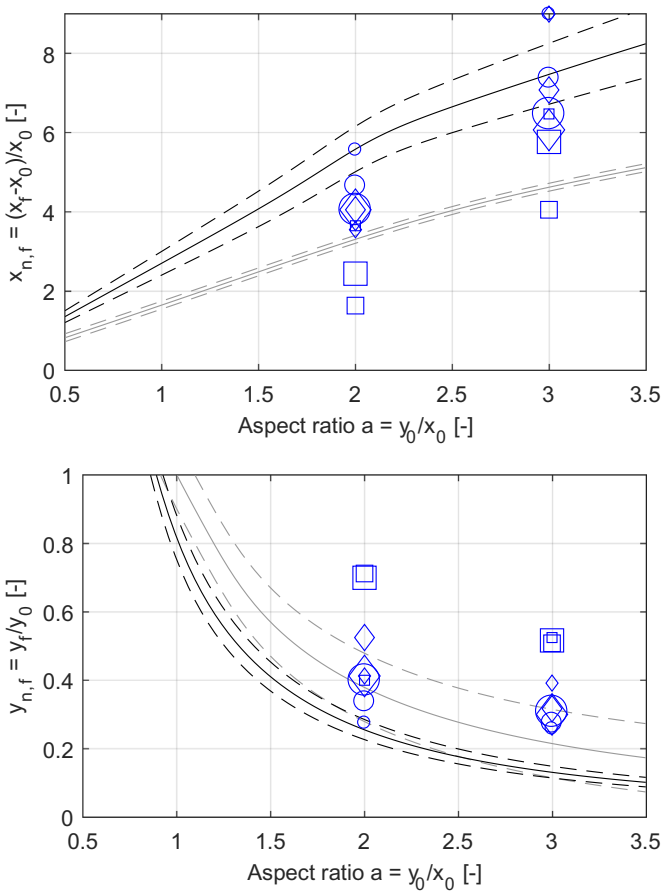

Fig. 5. Final non-dimensional run-out $x_{n,f}$ (left) and height $y_{n,f}$ (right) for sand in air with $\alpha_{s,0} \approx 0.59$. The data points correspond to the dimensional x_f and y_f values depicted in A.1.1. Grey solid lines represent the scaling of Lube et al. [3] with dashed lines indicating ± 10%, black solid lines the scaling of Bougouin and Lacaze [2] for the FFR with dashed lines indicating uncertainty given in [2].

simulation where obtained by letting a pile of sand settle in air in order to obtain steady and smooth fields for all quantities. Figs. 6 and 7 depict the dimensionless final run-out length and final deposit height for $\alpha_{s,0} = 0.55$ and $\alpha_{s,0} = 0.60$, respectively. Here, the IC were given by the constant $\alpha_{s,0}$ only, which was simply patched into the computational domain.

Most of the numerical run-out length data falls between the two scaling curves of Lube et al. [3] and Bougouin and Lacaze [2]. Exceptions are for instance the small particle diameters for the intermediate and large cliff scale for $a = 1$ in case of the patched solid volume fraction $\alpha_{s,0} = 0.55$ (Fig. 6 left) as well as the intermediate and large particle diameters for the large cliff scale for $a = 2$ in case of the pre-simulated solid volume fraction $\alpha_{s,0} \approx 0.5$ (Fig. 5 left).

Both exceptions are represented in the respective deposit height plots, were in case of the latter the data points fall above (Fig. 5 right) and in case of the former the data points fall below the scaling laws (Fig. 6 right).The deposit height data for the large cliff scale cases fall consistently on top of the scaling laws, i.e. the numerically obtained deposit height is always larger than the experimentally obtained as represented by the scaling laws.

For the non-dimensional run-out length $x_{n,f}$, some data points coincide at the maximum value. This is the end of the computational where solids where stopped by the boundary wall.

On a more general note, for a particular aspect ratio all results feature a spread in the order of up to ± ≈ 50% for the run-out distances and ± ≈ 50% for the deposit heights.

3.3. Sand in water

Fig. 8 provides the dimensionless final run-out length and final deposit height for $\alpha_{s,0} \approx 0.59$, i.e. where the IC conditions of the simulation where obtained by letting a pile of sand settle in air in order to obtain steady and smooth fields for all quantities. Figs. 9 and 10 depict the dimensionless final run-out length and final deposit height for $\alpha_{s,0} = 0.55$ and $\alpha_{s,0} = 0.60$, respectively. Here, the IC were given by the constant $\alpha_{s,0}$ only, which was simply patched into the computational domain.

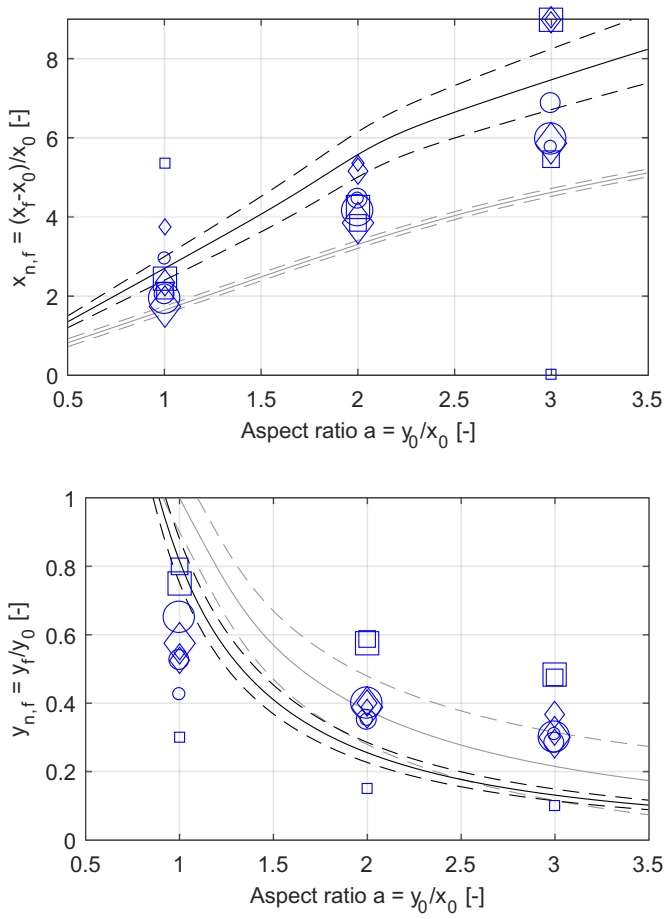

Fig. 6. Final non-dimensional run-out $x_{n,f}$ (left) and height $y_{n,f}$ (right) for sand in air with $\alpha_{s,0} = 0.55$. The data points correspond to the dimensional x_f and y_f values depicted in A.2.1. For further description see caption of Fig. 5.

In contrast to the air results, most of the numerical run-out length data is much more scattered. However, the majority falls between the scaling curves for the VR and the IR of Bougouin and Lacaze [2]. Exceptions are for instance the small particle diameters for $a = \{1, 2\}$ in case of the patched solid volume fraction $\alpha_{s,0} = 0.55$ (Fig. 9 left) as well as the small particle diameters in case of the pre-simulated solid volume fraction $\alpha_{s,0} \approx 0.59$ (Fig. 8 left).

The numerical results for the deposit height are much less scattered than the run-out length results, except for $a = 1$, where the small particle diameter data is only about 25% of the scaling law magnitude. Consistently, for all $\alpha_{s,0}$, the large particle diameter cases fall above, and the small particle diameter cases fall below the scaling laws. Furthermore, the large cliff scale (represented by squared boxes) produces the largest deposit heights, while the intermediate and small cliff scales (represented by diamonds and circles, respectively) produce smaller deposit heights and lie close together.

The corresponding dimensional results show that for some combinations, e.g. $\alpha_{s,0} \approx 0.59$ and $a = 2$, cases 1, 4, 7, 8 (Fig. A.11), the cliff has entirely disintegrated and the steady-state is a flat sediment bed. In some other cases, e.g. $\alpha_{s,0} \approx 0.59$ and $a = 3$, case 7 (Fig. A.12), it appears as if the simulation time was to short and no steady-state has been reached yet. For these two phenomena, our implementation of Eq. (38) has difficulties capturing the final run-out length correctly, as may be seen from e.g. $\alpha_{s,0} \approx 0.59$ and $a = 2$, case 4 (Fig. A.12).

While the scaling laws state that the VR run-out lengths are shorter than the IR ones, this is not represented by the numerical data. As depicted on Fig. 4, the intermediate and large particle diameters cases fall into the IR and the small ones into the viscous regime. However, the order of the run-out length depicted on Figs. 8–10 is vice-versa in most cases when compared to the respective scaling laws.

The same applies to the deposit heights, where small diameters almost consistently feature the smallest deposit heights. However, as opposed to the run-out lengths the virtual difference between the deposit height scaling laws for the IR and VR is negligible.

3.4. Sand in PAC

For PAC, the same observations can be made as for the previously discussed water cases. However, the scatter of the data is worse. Hence, we only briefly summarize the major points of the PAC results[8]:

Many of the PAC2 results also fall between the two scaling laws for the run-out length. The large particle diameter cases produce deposit heights larger than what the scaling law predicts, and the order of the numerical results does not reflect the order of the flow regime dependent scaling laws.

An entirely leveled-out sediment bed also occurs for the small particle diameter cases. The not-occurred disintegration of the cliff occurs for almost the same cases.

3.5. Initial conditions in case of $\alpha_{s,0} \approx 0.59$

For all the cases $\alpha_{s,0} \approx 0.59$, i.e. where the IC conditions of the simulation where obtained by letting a pile of sand settle in the respective fluid in order to obtain steady and smooth fields for all quantities, the obtained fields showed a very inconsistent picture when it comes to smoothness.

For instance, in cases of the liquids where the cliff collapsed entirely and eventually yielded a horizontal deposit, initial conditions obtained by settling solids in a granular column do not feature a smooth frictional viscosity field. Fig. 11 depicts contour plots of the frictional viscosity, granular pressure and granular temperature at $t = 4$ s for $a = 2$ and case 1.

While the latter two appear smooth, the frictional viscosity shows regions of comparatively low viscosities in the lower center part and walls of the granular column and especially at the top of the bed.

3.6. Non-zero velocity at top of sediment bed

For all cases investigated, including the pre-simulations to obtain IC in case of $\alpha_{s,0} \approx 0.59$, the top-cells of the steady-state5F[9] sediment bed features a non-zero solid velocity, regardless of how long simulations are ran. Zooming in on the near-bed region of a pre-simulation as depicted in Fig. 12, it becomes clear that some of the cells feature a positive vertical solid velocity.

These are corelated with large changes of the kinetic/collisional solid pressure $p_{s,k/c}$, as shown in Fig. 12 (right) or more in Fig. B.7 in Appendix B, which shows the y-component of the gradient of the kinetic/collisional solid pressure $p_{s,k/c}$ displayed in Fig. 12 (right).

A more comprehensive set of field plots covering all relevant quantities is provided in Appendix B.

4. Discussion

At first glance, the numerical results appear to not scale well with the scaling laws of Lube et al. [3] and Bougouin and Lacaze [2]. In the following, we will first discuss the issue of non-zero velocities at the top of the deposit bed, which overshadows the results, and provide potential

[8] See https://www.youtube.com/playlist?list=PLfeJTTWUNqAXyvNppPBEMm5_I531YQV2p for some PAC2 CCP results and https://www.youtube.com/playlist?list=PLfeJTTWUNqAUFGIO9Gz-wFzHJxmTg1-cm for some PAC4 CCP results.

[9] Here steady-state is a relative term as the discussion will show. For now, it refers to the final state as obtained in the simulations at maximum flow time. More generally, and with respect to real world experiments, it is a state, where the deposit flow has completely stopped and the final shape is a deposit slope.

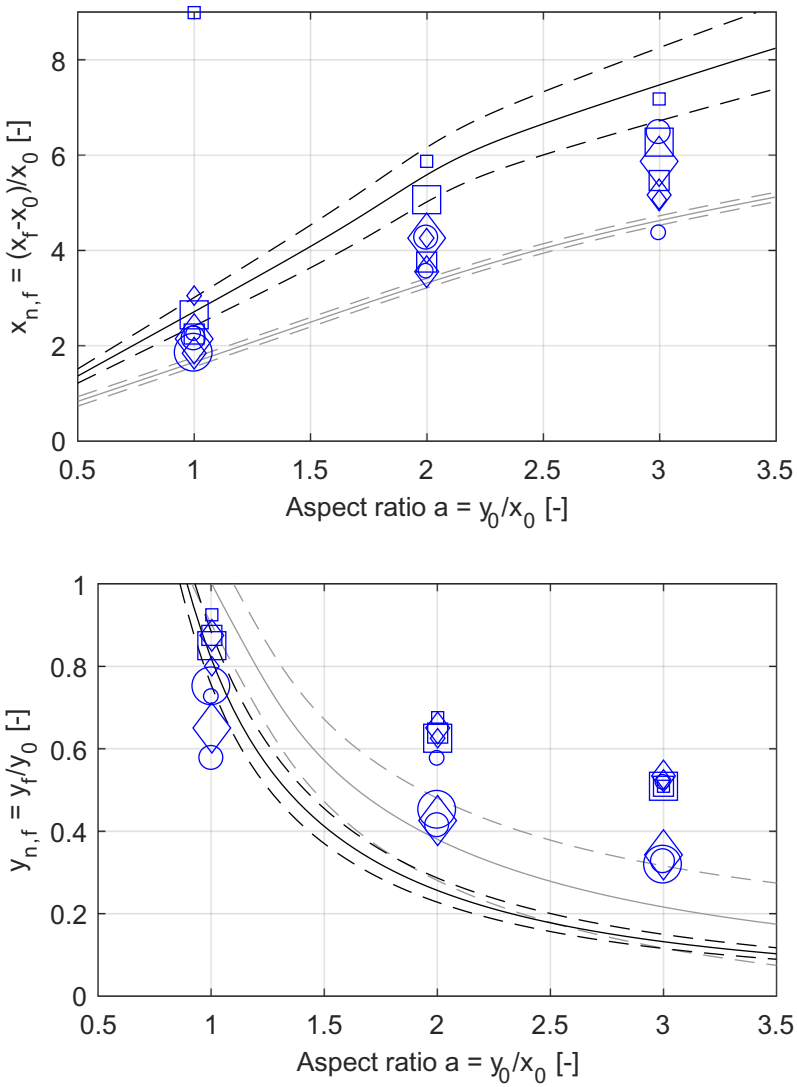

Fig. 7. *Final non-dimensional run-out $x_{n,f}$ (left) and height $y_{n,f}$ (right) for sand in air with $\alpha_{s,0} = 0.60$. The data points correspond to the dimensional x_f and y_f values depicted in A.3.1. For further description see caption of Fig. 5.*

explanations linked to the computational procedure. After briefly focusing on the relevance of the utilized closures laws for the solid stress tensor, we discuss the numerical results with respect to the scaling laws of Lube et al. [3] and Bougouin and Lacaze [2]. Finally, we comment on the applicability of the employed modeling approach for hydraulic conveying applications such as cuttings transport in wellbores and dune migration.

4.1. Non-zero velocity at top of bed

Because of the non-zero velocity in the grid cells at the top of the deposit bed, the entire top-layer of the granular bed remains in a—in the framework of the TFM—low-viscosity-like state and thus keeps flowing over long periods of time. Hence, the non-zero velocity in the grid cells close to the top of the deposit bed is affecting the final run-out length and deposit height because solids are continuously redispersed into the fluid layer on top of the sediment bed and settle back down. The top-layer of the sediment bed is a region of high shear and thus the frictional viscosity is very low leading to the top layer of the sediment bed remaining in a low-viscosity-like state, regardless of the total simulation time. In case of the cliff collapse problem, this leads to a small but continuous downslope flow of sediment, which over longer time scales further reduces the deposit height and consequently increases the run-out length. It is important to realize that this hereafter called *top bed velocity defect* not only avoids a steady-state (The system does not really reach a true steady-state as the top layer of the granular bed remains in a dynamic state) but also affects the dynamics of the granular collapse by a small degree.

The reason for this positive solid velocity component as shown in Fig. 12 is the internal switching of Fluent when it comes to the computation of the solid stress tensor, namely Eq. (28): For cells where $\alpha_s < \alpha_{s,f} = 0.5$, only the kinetic/collisional part $\mathbf{T}_{s,k/c}$, is computed and the frictional part $\mathbf{T}_{s,f}$ is zero, i.e., the solid phase in these cells is not subject to the frictional models as given by eqs. (35) and (36), and is only governed by the KTGF. However, the non-consideration of the frictional viscosity $\eta_{s,f}$ leads to very low values of the solid viscosity η_s and thus results in a liquid-like state of the solids phase. Apparently, in these cells the solid pressure gradient $\nabla p_{s,k/c}$ (which is determined based on Eq. (31) and not by pressure-velocity coupling) is then large enough to overcome the effect of gravity and provide enough momentum to lift the solids.

In case of an inclined bed, for instance the states of the cliff collapse system after collapse and when reaching a first quasi steady state where the deposit shape features an angle of repose, α_s in the top layer cells may have any numerical value between 0 and $\alpha_{s,mpd}$ because the cell is not necessarily entirely filled with the dense bed. While this is

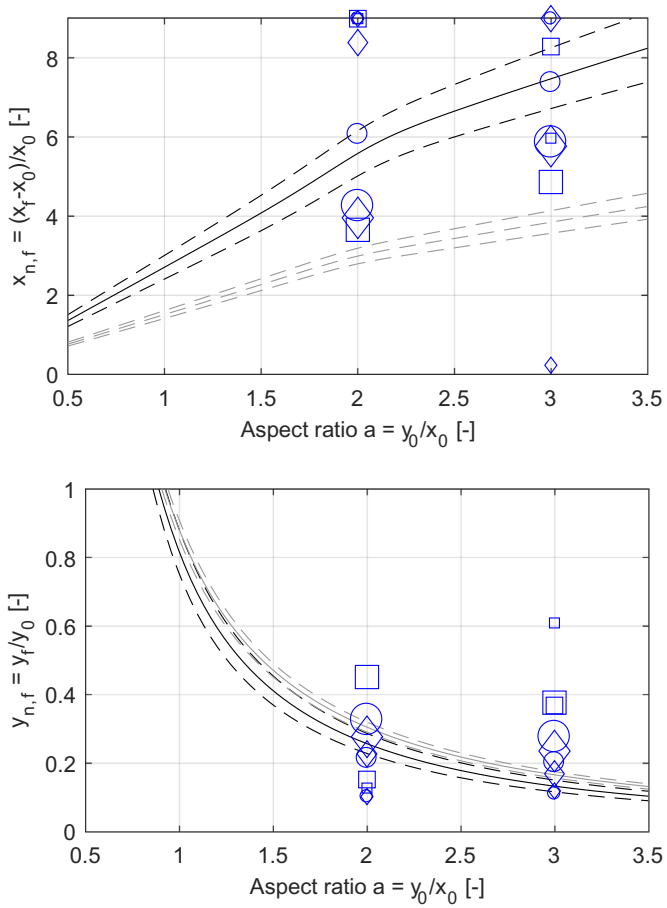

Fig. 8. Final non-dimensional run-out $x_{n,f}$ (left) and height $y_{n,f}$ (right) for sand in water with $\alpha_{s,0} \approx 0.59$. The data points correspond to the dimensional x_f and y_f values depicted in A.1.2. Grey solid lines represent the scaling of Bougouin and Lacaze [2] for the VR and black solid lines the scaling of Bougouin and Lacaze [2] for the IR, with dashed lines indicating uncertainty given in [2], respectively.

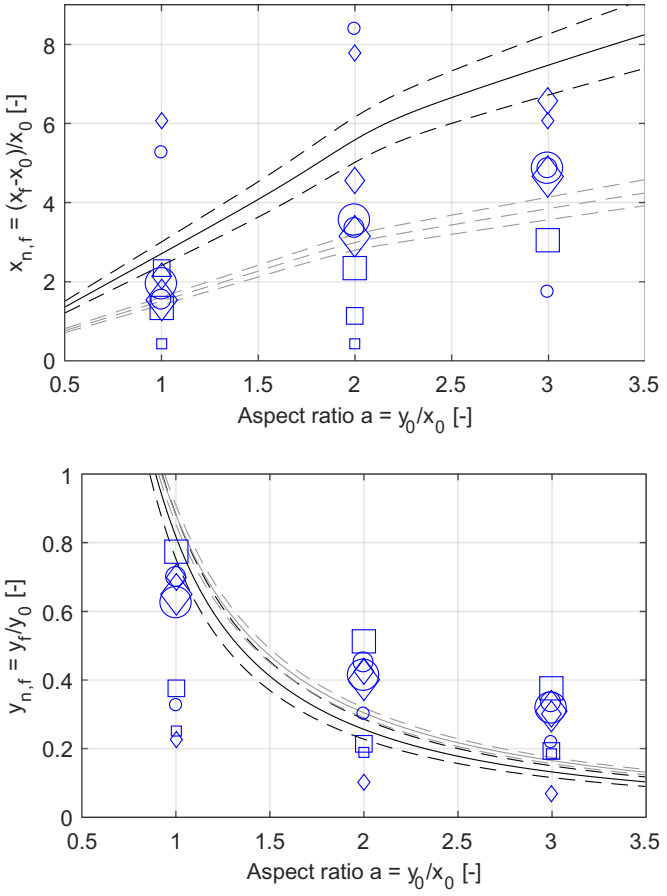

Fig. 9. Final non-dimensional run-out $x_{n,f}$ (left) and height $y_{n,f}$ (right) for sand in water with $\alpha_{s,0} = 0.55$. The data points correspond to the dimensional x_f and y_f values depicted in A.2.2. For further description see caption of Fig. 8.

perfectly representing the current shape of the deposit for the current point in time, the numerical values lead to a granular rheological behavior entirely governed by the KTGF because the frictional closures are only activated for $\alpha_s > \alpha_{s,fric} = 0.5$. Hence this top layer sees some self-induced flow due to the KTGF-governed cells.

4.2. Computational procedure

In order to better understand the described *top bed velocity defect* phenomena, we tried alternative numerical approaches such as implicit and explicit volume fraction treatment and the coupled (including coupled with volume fractions) solving approach. However, the same *top bed velocity defect* occurred. Letting the solver compute two volume fractions instead of exploiting constraint (13) led to divergence. Disactivating the KTGF state equation for the solid pressure, i.e. Eq. (31), led to a significant reduction of the *top bed velocity defect*. The granular temperature decreased significantly to very low levels.

Therefore, our hypothesis is that the observed phenomena is due to a checker-board-like issue arising in the multiphase pressure-velocity-coupling (PVC) concept employed by Fluent on a collocated grid which does not fully account for the KTGF solid pressure. While details of the "Rhie and Chow type of scheme to calculate volume fluxes" are not disclosed [45,46], it appears that volume fractions are held constant and the shared pressure is used as a basis. However, the Rhie and Chow interpolation procedure [47] used to compute the normal flux velocity components on the cell faces is known to produce collocated velocities under certain circumstances e.g. the presence of strong body forces such as when explicit solid pressure or gravity become strong [48]. In the top-layer region where the *top bed velocity defect* occurs, the solid pressures (31) and (35), which act as source term in the momentum equations, are strongly dependent on the solid volume fraction and hence should be considered in the pressure corrections step [48].

In earlier versions of Fluent, a second pressure correction equation appears to have been solved for the solid pressure [28,49]. In that case, the introduction of the additional state equations $p_s = p_{s,c/k}(\alpha_s,\ldots) + p_{s,f}(\alpha_s,\ldots)$ results in an overdetermined system [28]. Obtaining α_s from p_s instead is one way to remedy this problem [28] and led to the Compressible Disperse Phase (CDP) method, which was effectively applied to simulate the hour glass problem without any *top bed velocity defect* phenomena and staple slopes of granular heaps [28]. Later, it was unsuccessfully attempted to implement the CDP method using a co-located mesh (A collocated mesh lead to negative pressures for some solid volume fractions, while a staggered arrangement ensured positivity for all solid fractions) [50].

More recently, Passalacqua and Fox [51] and Venier et al. [52] developed numerical approaches to handle granular flows for the open-source CFD code OpenFoam, where the particle pressure contribution to the solid flux is considered and two phasic pressure correction equations are solved. Both successfully employed a settling bed of solids as test case, however, only solid volume fraction and no velocity plots were disclosed.

An alternative explanation for the observed phenomena is the concept of numerical storms due to unbalanced numerical schemes [53]. Well-balanced here refers to the property of conserving the

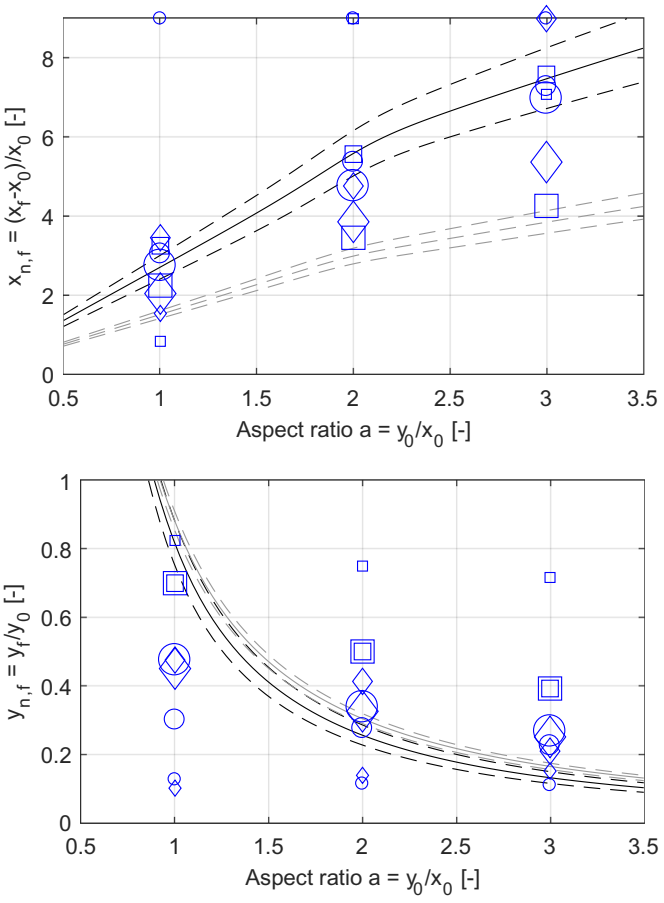

Fig. 10. Final non-dimensional run-out $x_{n,f}$ (left) and height $y_{n,f}$ (right) for sand in water with $\alpha_{s,0} = 0.60$. The data points correspond to the dimensional x_f and y_f values depicted in A.3.2. For further description see caption of Fig. 8.

fundamental balance of hydrostatic pressure and gravitational acceleration down a slope at steady-state at a discrete level [53]. If this is not the case, it can be shown that for the shallow-water equations, a lake at rest will feature spurious oscillations of the water surface [53]. A much finer grid will help to minimize the numerical artefacts and may correspondingly be beneficial in reducing the order of magnitude of the velocity defect seen in our simulations.

4.3. Relevance of solid closure laws

The form of the stress tensor, namely Eq. (28), in combination with the closure law for viscosity, namely Eq. (36), must allow a quasi-static solution, where the fluid is so highly viscous that it does not flow with respect to our time scales 1..0.100 s. For vanishing shear rates in the frictional regime, a Bingham-type flow behavior is obtained due to the yield feature inherent in Eq. (36). For instance, for the thin layer flow at the top of the sediment, u_s becomes smaller with a decreasing bed slope and thus also the shear rate and the stress become small. However, the viscosity η_f is based on the magnitude of the deformation rate tensor **D** in the denominator whereas a particular stress component of the stress tensor **T** is a direct function of the corresponding component of **D**. Now, the magnitude of **D** is always larger than the magnitude of the individual components of **D**, which eventually should lead to the cut-off viscosity (default cut-off value 10^5 Pa·s in Fluent) and to the above mentioned quasi-static state.

Another relevant factor contributing to the observed flowing state of the deposit top layer may be the combination of frictional viscosity and frictional pressure models describing the solid phase in dense regions. Venier et al. [52] showed that the application of the Schaeffer frictional model [23] in combination with the solid frictional pressure formulation of Syamlal et al. [22] produces much higher levels of solid volume fraction in the region just below the sediment top-layer, with a very sharp drop at the top of the sediment bed. Venier et al. [52] distinguish between the

- "Schaeffer model" (the solid frictional pressure formulation of Syamlal et al. [22] in combination with the frictional viscosity model of Schaeffer [23] as employed in this study).
- "Johnson and Jackson model" (the solid frictional pressure model of Johnson and Jackson [21] as employed in this study and the frictional viscosity model of Johnson and Jackson [21] which, in contrast to the model of Schaeffer [23], is independent of the shear rate).

However, it is the solid pressure formulation which in fact makes the difference because the solid frictional pressure formulation of Syamlal

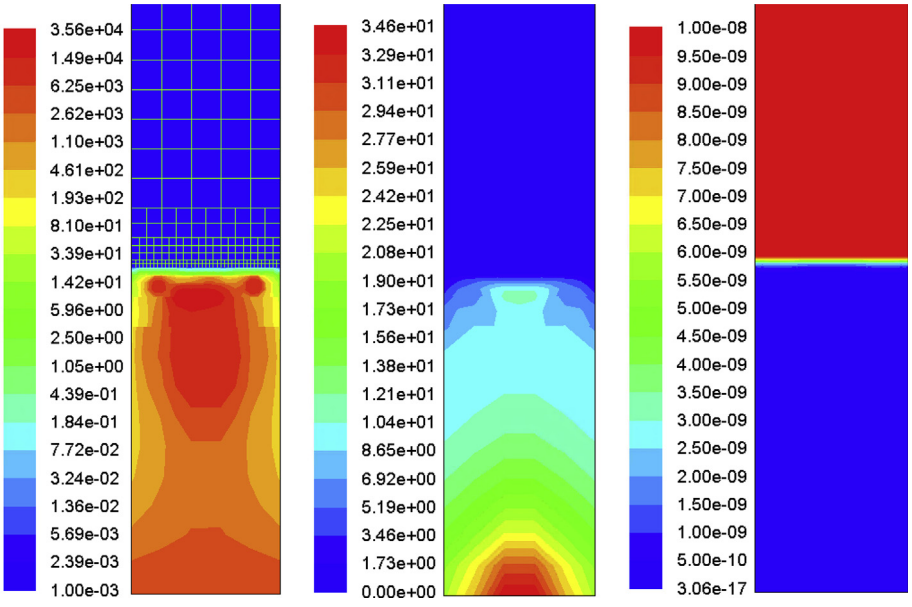

Fig. 11. Result of pre-simulation ($t = 4$ s for air, $a = 2$, case 1), from left to right: frictional viscosity, granular pressure, granular temperature.

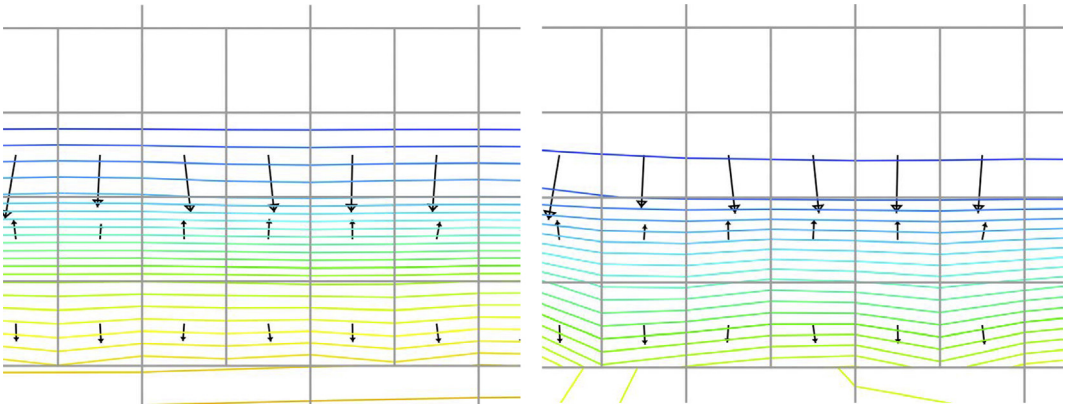

Fig. 12. Zoom of the top-bed region of the pre-simulation of air #5, air, a = 3 (For full field plots see Fig. B.1 and Fig. B.6 in Appendix B). Black arrows denote solid velocity. Left: Colored horizontal lines represent constants of solid volume fraction. Right: Colored horizontal lines represent constants of kinetic/collisional solid pressure.

et al. [22] diverges to levels of several magnitudes larger than the one of Johnson and Jackson [21]. Hence, the combination of the solid frictional pressure formulation of Syamlal et al. [22] and the frictional viscosity model of Schaeffer [23] may be a viable option in order to decrease the magnitude of the liquid-like state of the solid phase below the top of the sediment bed. However, the frictional pressure formulation of Syamlal et al. [22] is available as a solid frictional pressure model in Fluent but its application does also lead to the velocity field disturbance at the top of the sediment bed, as described in sections 3.7 and 4.1.

If an alternative material function is utilized for the frictional viscosity, for instance the one put forward by Laux [28], heap building is generally enhanced because the material functions of Laux and the one Schaeffer [23] differ by one order of magnitude.

4.4. Numerical results vs. scaling of experimental data

Major factors affecting the comparison of numerical and experimental results are:

- The previously mentioned *top bed velocity defect* which leads to an ongoing flow of the outer layer after the deposit has reached a first quasi steady-state similar to the angle of repose of the material. This flow continuously decreases the deposit height, increases the run-out length and ultimately leads to an entirely flat bed for sufficiently long flow times.
- Factors not taken into account in the scaling laws of of Bougouin and Lacaze [2] and Lube et al. [3] such as the materials angle of internal friction, the particle diameter and the scale of the cliff as well as initial conditions.
- The performance of the closures, in particular the frictional pressure and stress models, utilized to describe the solid phase.

If the solid phase is simply patched into the domain, it is crucial to identify the solid volume fraction of the model which relates to the solid volume fraction in the real world. In case of water as the interstitial fluid, the collapse happens in about 2–3 s. For a liquid first phase, the initial solid volume fraction of the cliff is known to have a drastic effect on the dynamics of the collapse [10]. From a logical standpoint, our results obtained with the pre-simulated settled solid bed in dynamic equilibrium ($\alpha_{s,\,0} \approx 0.59$) and more so our $\alpha_{s,\,0} = 0.60$ results are equivalent with the loose solid bed ($\alpha_{s,\,0} \approx 0.55$) of Rondon et al. (2011) [10] because the plain settling of solids in our numerical pre-simulation is precisely how Rondon et al. (2011) [10] obtained the initial granular column in their experiments. Hence, the numerical model needs to be tuned such that the pre-simulations result in settled beds with $\alpha_{s,\,0} \approx 0.55$, for instance by adjusting the maximum packing density $\alpha_{s,\,mpd}$ and the beginning of the frictional regime $\alpha_{s,\,f}$.

Now, considering our $\alpha_{s,\,0} = 0.55$ results, the full collapse of the small particle size cliffs may be explained by the fact that the $\alpha_{s,\,0} = 0.55$ in our simulations corresponds to an unsettled and hence uncompacted state in the real world. Therefore, in the framework of the model, no significant frictional viscosity build-up could occurs within the time scale of the collapse. Frictional viscosity builds up over time because of the developing compaction process in the remaining cliff. This process occurs on a certain time scale as the liquid must flow out of the bed. This outflow process takes much longer in case of smaller particles because the Stokes settling velocity scales with the square of the particle diameter and so does the permeability of a packed bed of solids. Hence, flow dynamics are governed by the liquid because of the low Stokes numbers and the collapse of the granular column is thus dominated by fluid inertia rather than the particles itself. Once liquid is ejected from the granular pile and the granular collapse occurs small particles do have insufficient inertia to resist the liquid flow and counteract the collapse. The build-up of frictional pressure and thus frictional viscosity does not occur sufficiently within the time scale of the collapse. The granular media thus remains in a flowing state and may level out prior to reaching sufficient frictional viscosity levels to represent the Mohr-Coulomb yield criterion inherent in the Schaeffer [23] frictional viscosity model. The role of particle and fluid inertia also explains the different order of the various particle diameter results when compared to the VR and IR scaling laws: Smaller particles follow the flow and therefore less deposit height and smaller run-out length may occur.

Therefore, to first compact the solid phase under the pure influence of gravity is the preferred strategy to obtain correct IC, with sufficiently accurate profiles of volume fraction, solid pressure, and frictional viscosity. The failure of these in some simulations is attributed to the aforementioned *top bed velocity defect*, which, as shown in Fig. 11, may negatively affect the solid frictional viscosity field.

Various spatial scales seem to lead to different non-dimensional deposit heights and run-out lengths. Apparently, these two quantities are not universal for a given granular material in the utilized modeling framework. The *top bed velocity defect* is contributing to this effect because the ratio of the outer layer flow thickness to the scale of the cliff varies. In addition, the frictional pressure may also play a role. In case of larger spatial scales, a more compacted bed is produced which then yields higher average levels of the frictional viscosity. For instance, $\alpha_{s,\,pack}$, defined as the maximum packing density observed in the entire domain, is larger for large systems ($\alpha_{s,\,pack} \approx 0.625$) and smaller for smaller systems ($\alpha_{s,\,pack} \approx 0.605$). As the build-up and break down of the frictional viscosity occurs on time scales in the order of the initial collapse of the cliff, the different average frictional viscosity levels may also contribute to the cliff scale being a factor.

The scaling laws are based on 3D experiments in a channel and may thus be affected by the *z*-dimension in terms of friction between particles and the channel side walls. The 2D simulations assume an infinitely wide channel.

With all these factors in mind, the performance of the numerical model is much better than it seems at first glance. While in its present form it does not allow accurate quantitative predictions of the final run-out length and final deposit height it may be tuned with regards to the solid frictional pressure and frictional viscosity formulations as well as numerical coefficients such as the angle of internal friction to yield better quantitative results. However, the time-dependency of the results due to the *top bed velocity defect* remains an issue and needs further attention.

4.5. Consequences for modeling of hydraulic conveying

In general, the TFM-KTGF modeling framework as utilized in this study seems capable of modeling hydraulic conveying on a qualitative basis. However, due to several factors such as the *top bed velocity defect* as well as the required tuning of model parameters, quantitative results will most likely be incorrect. Especially the artificial agitation of the bed surface will lead to an overestimation of transported solids. Presence of flow will thus immediately result in transport of solids in the streamwise direction although physics dictate a critical value of bed shear stress to be exceeded to mobilize grains and transport solids. For the very same reason, modeling of dune migration is not adequately possible, at least on larger time scales. While the occurrence of reverse flow at the lee side of the dune may help to sustain the dune shape, the *top bed velocity defect* will cause a disintegration of the dune over extended flow times.

5. Conclusions & outlook

We have investigated the CCP for different fluids, initial solid volume fractions, aspect ratios as well as particle and cliff scale combinations with the TFM-KTGF-SM framework.

At steady-state, the model does not yield an accurate physical representation of a stable deposit close to the angle of repose of the material. Instead, a thin layer at the top of the sediment remains flowing, yielding a scale-dependent disintegration of the cliff over longer periods of time. We suspect this phenomenon to be a consequence of the numerical solutions strategy of Fluent which may result in some solid flux imbalance at top-bed regions where the gradient of the solids kinetic/collisional pressure is high.

Model tuning based on calibration of parameters (angle of internal friction, solid volume fraction threshold for the frictional regime, maximum packing density) and possibly alternative closures for both solid frictional pressure and solid viscosity are required to match the solid volume fraction of the model with the solid volume fraction of the real world and better replicate the experimental data. On the other hand, experimental spread and missing experimental data for the shear-thinning fluids require more comprehensive experimental data for validation purposes.

If the model in its current form is used for transport modeling of cuttings in wellbore flows, the *top bed velocity defect* will lead to an unknown overestimation of transported solids. When it comes to the modeling of dune migration, the *top bed velocity defect* will likely cause disintegration of the dune over longer periods of time.

Declaration of Competing Interest

None.

Acknowledgements

The project Advanced Wellbore transport Modeling (AdWell) with its sponsor, PETROMAKS 2/the Research Council of Norway (project 228391) and its partners Equinor, Neptune Energy AS, IRIS, UiS, NTNU and SINTEF are gratefully acknowledged for funding and supporting this work. In addition, we are very grateful for the computational resources provided at NTNU by UNINETT Sigma2 AS, as part of the national infrastructure for computational science in Norway. Finally, we thank Tore Halsne Flåtten for his input on the numerical part.

Appendix A. Dimensional final deposit shapes

A.1. Initial solid volume fraction $\alpha_{s,0} \approx 0.59$

A.1.1. Air

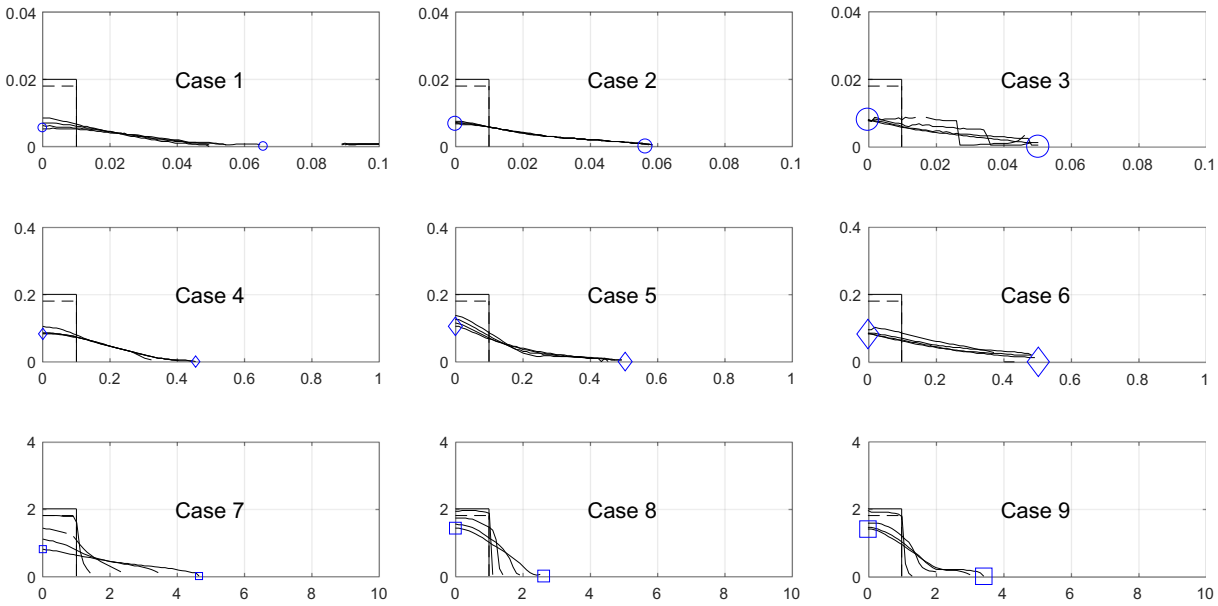

Fig. A.1. Time evolution of dimensional shapes (x and y positions of the cliff boundary) of sand in air for initial solid volume fraction $\alpha_{s,0} \approx 0.59$ and aspect ratio $a = 2$ as given by Table 3. The individual shapes represent the collapsing cliff at $t = 0, 1, 2, 3, 4$ s. The final values of $x_f = x(t = 4\text{ s})$ and $y_f = y(t = 4\text{ s})$ *are highlighted and correspond to the values depicted in* Fig. 5.

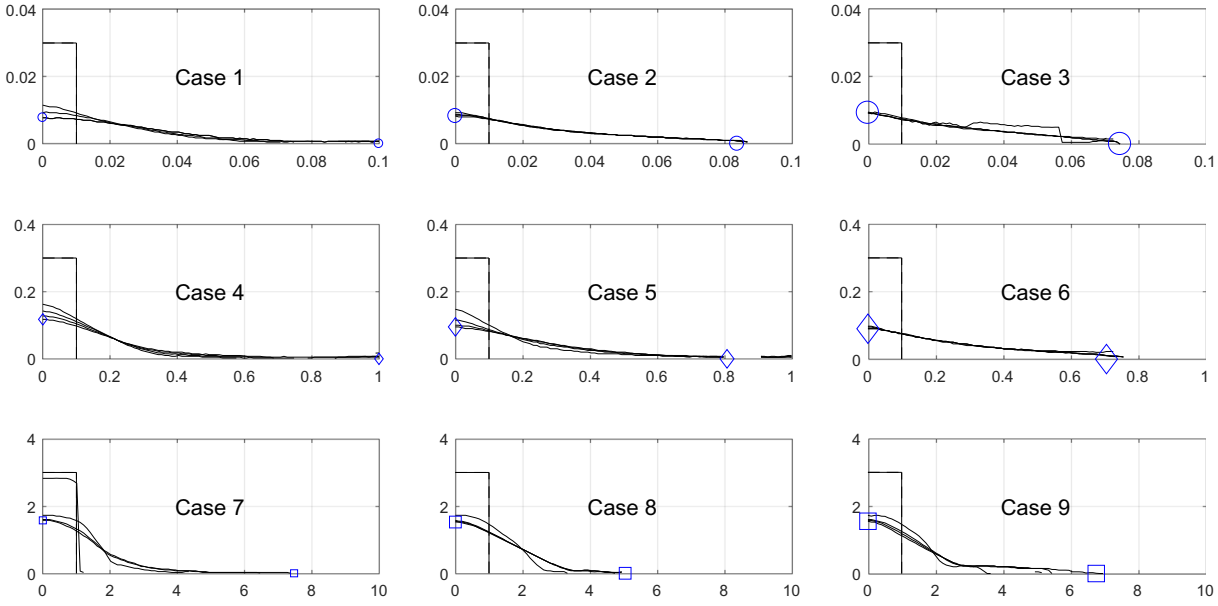

Fig. A.2. Time evolution of dimensional shapes (x and y positions of the cliff boundary) of sand in air for initial solid volume fraction $\alpha_{s,0} \approx 0.59$ and aspect ratio $a = 3$. For further description see caption of Fig. A.1. *Videos available here: https://www.youtube.com/playlist?list=PLfeJTTWUNqAWQZ6mgCWEXgR7_IpCQdfOo.*

A.1.2. H2O

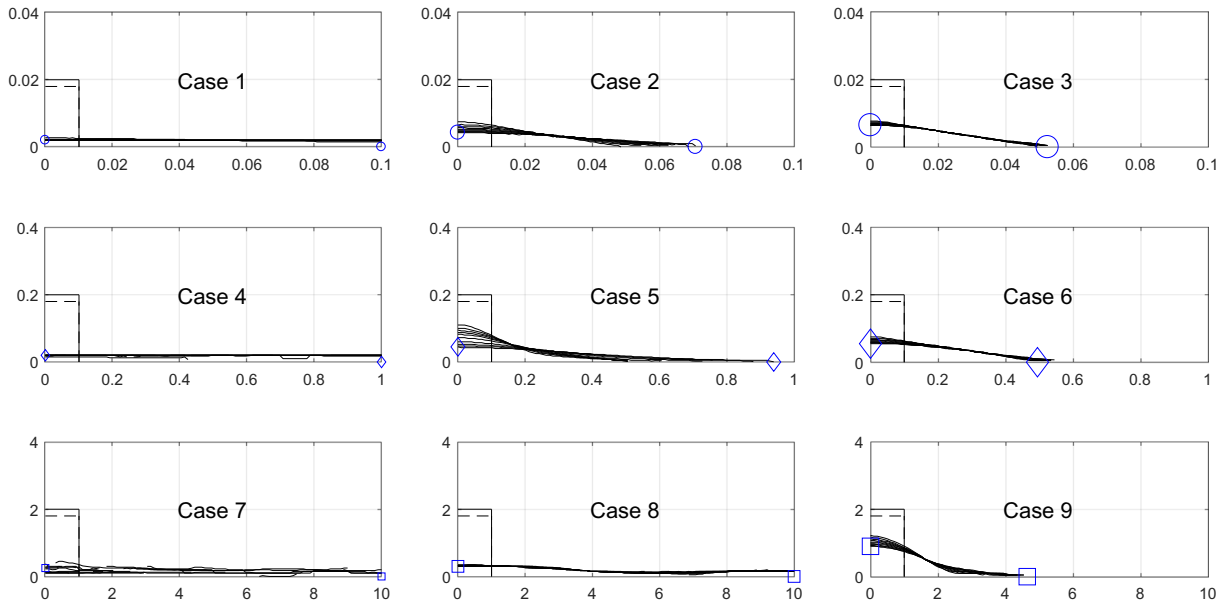

Fig. A.3. Time evolution of dimensional shapes (x and y positions of the cliff boundary) of sand in water for initial solid volume fraction $\alpha_{s,0} \approx 0.59$ and aspect ratio $a = 2$ and the different cases as given by Table 3. The individual shapes represent the collapsing cliff at $t = 0, 10, 20, \ldots, 100$ s. The final values of $x_f = x(t = 100\ \text{s})$ and $x_f = y(t = 100\ s)$ *are highlighted and correspond to the values depicted in* Fig. 8.

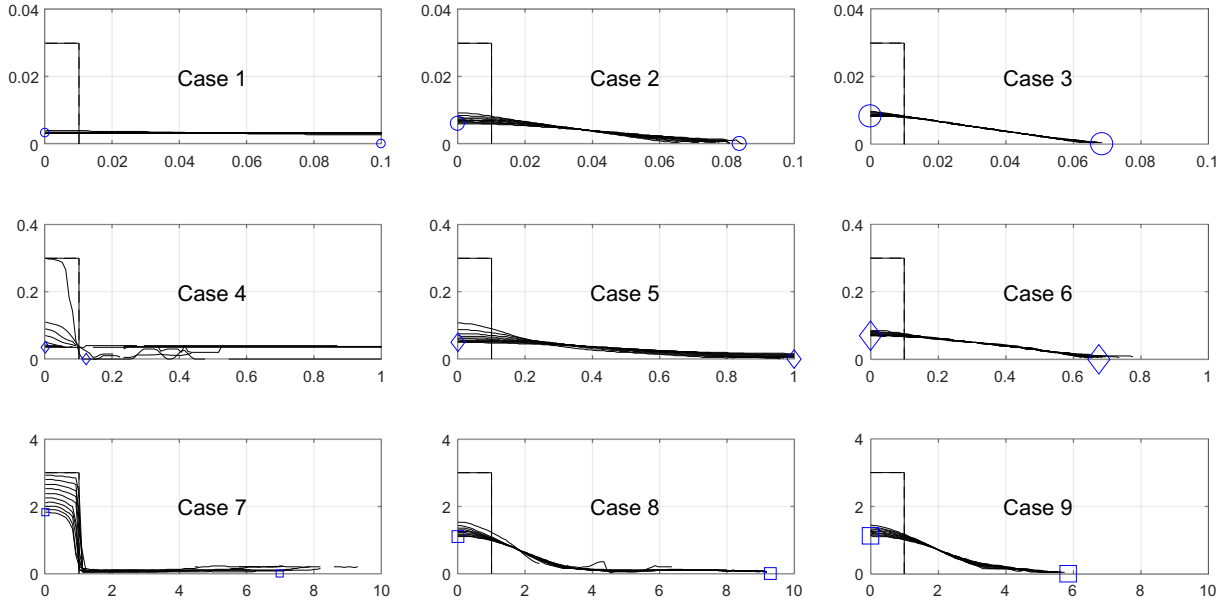

Fig. A.4. Time evolution of dimensional shapes (x and y positions of the cliff boundary) of sand in water for initial solid volume fraction $\alpha_{s,0} \approx 0.59$ and aspect ratio $a = 3$. For further description see caption of Fig. A.3. *Videos available here.: https://www.youtube.com/playlist?list=PLfeJTTWUNqAVyrW3M9QMmxhN9v3jz9knq.*

A.2. Initial solid volume fraction $\alpha_{s,0} = 0.55$

A.2.1. Air

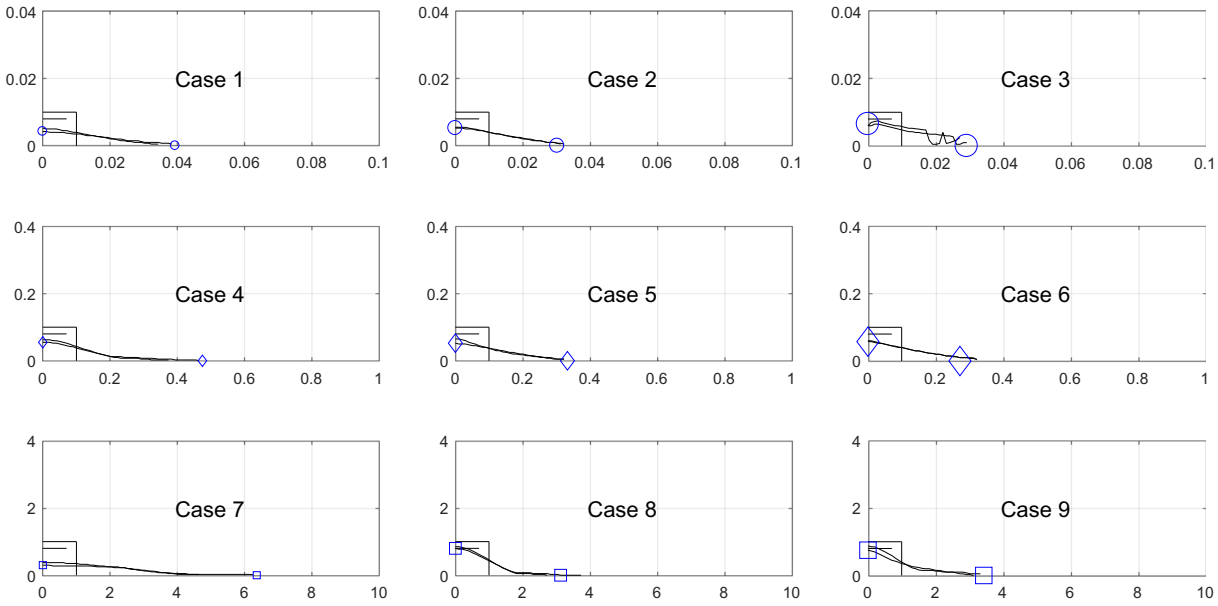

Fig. A.5. Time evolution of dimensional shapes (x and y positions of the cliff boundary) of sand in air for initial solid volume fraction $\alpha_{s,0} = 0.55$ and aspect ratio $a = 1$ and the different cases as given by Table 3. The individual shapes represent the collapsing cliff at $t = 0, 1, 2$ s. The final values of $x_f = x(t = 2\,s)$ and $y_f = y(t = 2\,s)$ *are highlighted and correspond to the values depicted in* Fig. 6.

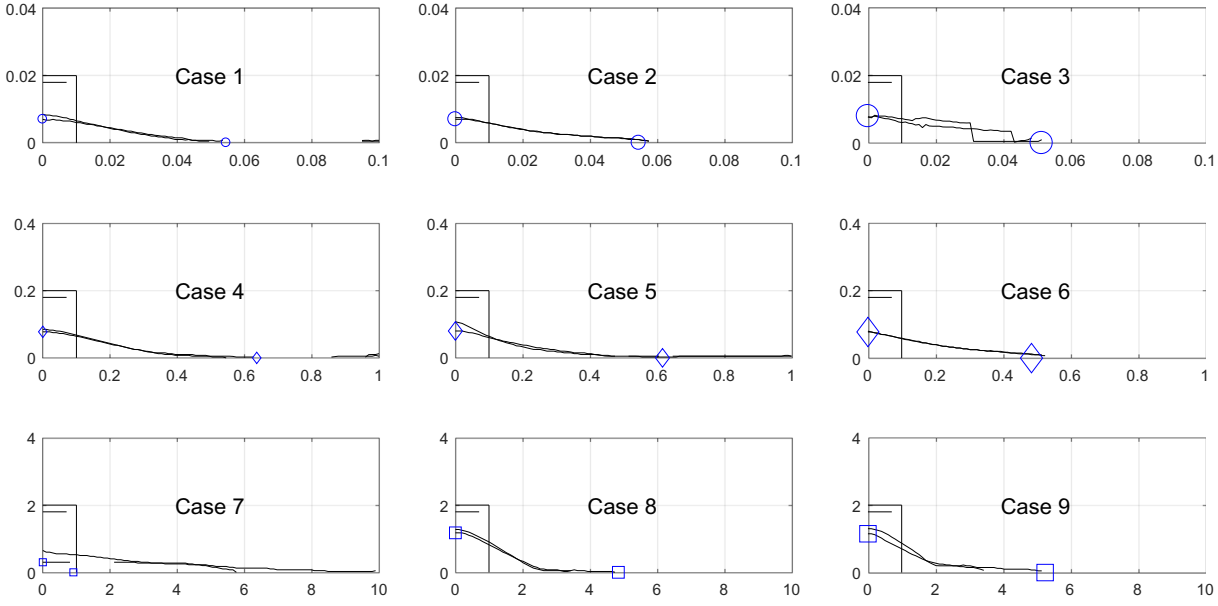

Fig. A.6. Time evolution of dimensional shapes (x and y positions of the cliff boundary) of sand in air for initial solid volume fraction $\alpha_{s,0} = 0.55$ and aspect ratio $a = 2$. For further description see caption of Fig. A.5.

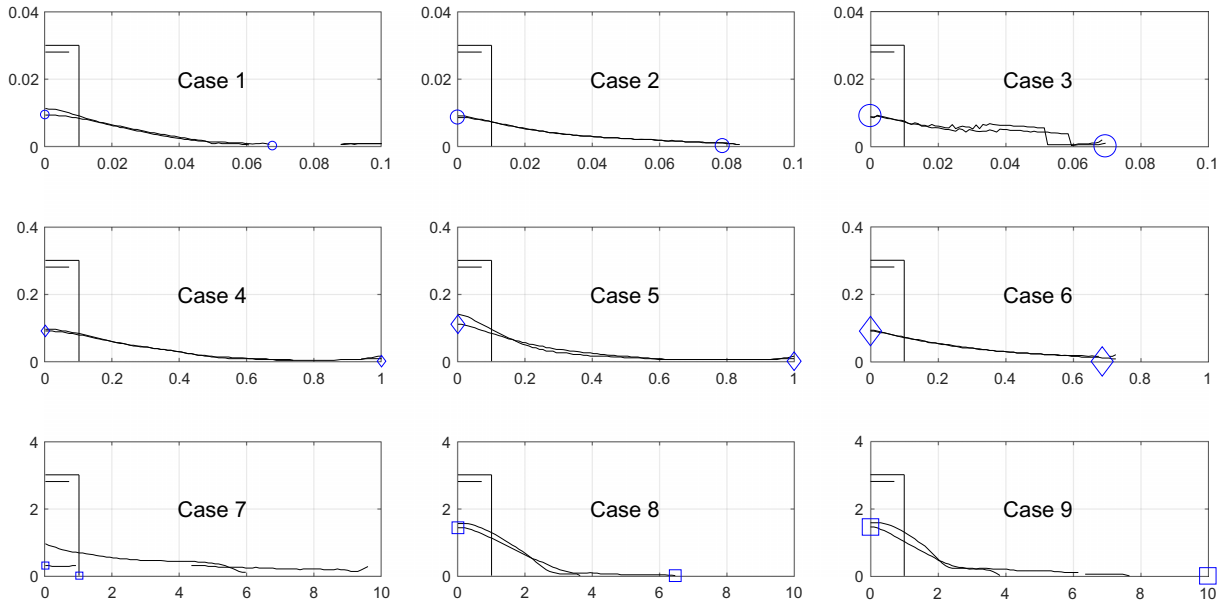

Fig. A.7. Time evolution of dimensional shapes (x and y positions of the cliff boundary) of sand in air for initial solid volume fraction $\alpha_{s,0} = 0.55$ and aspect ratio $a = 3$. For further description see caption of Fig. A.5.

A.2.2. H2O

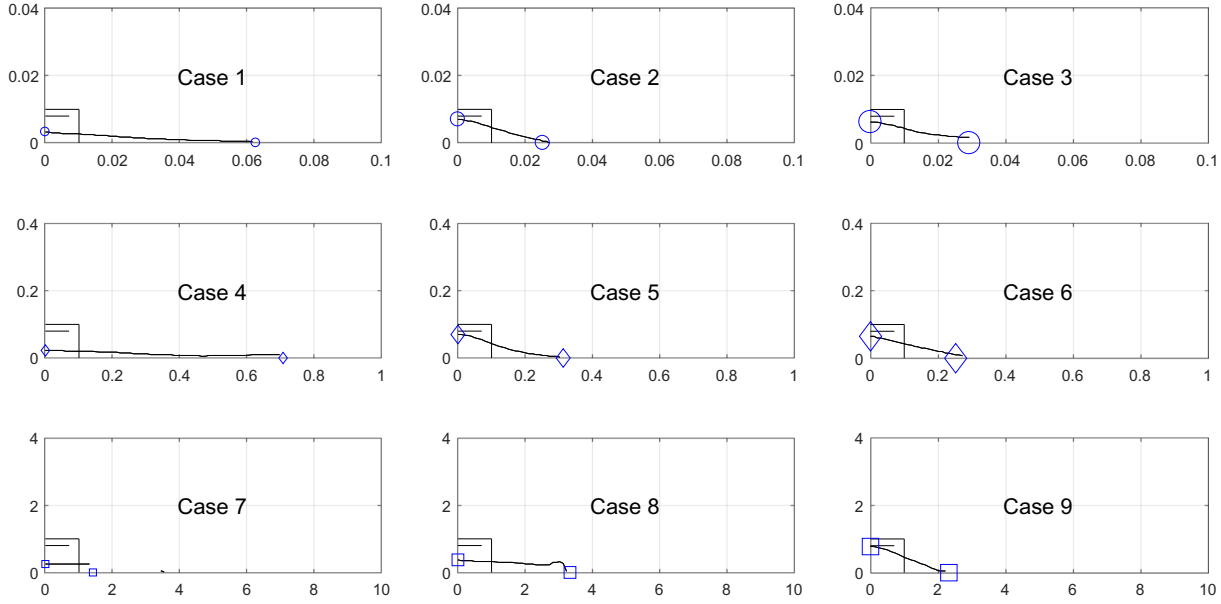

Fig. A.8. Time evolution of dimensional shapes (x and y positions of the cliff boundary) of sand in water for initial solid volume fraction $\alpha_{s,0} = 0.55$ and aspect ratio $a = 1$ and the different cases as given by Table 3. The individual shapes represent the collapsing cliff at $t = 0, 1, 2$ s. The final values of $x_f = x(t = 2\text{ s})$ and $y_f = y(t = 2\text{ s})$ *are highlighted and correspond to the values depicted in* Fig. 9.

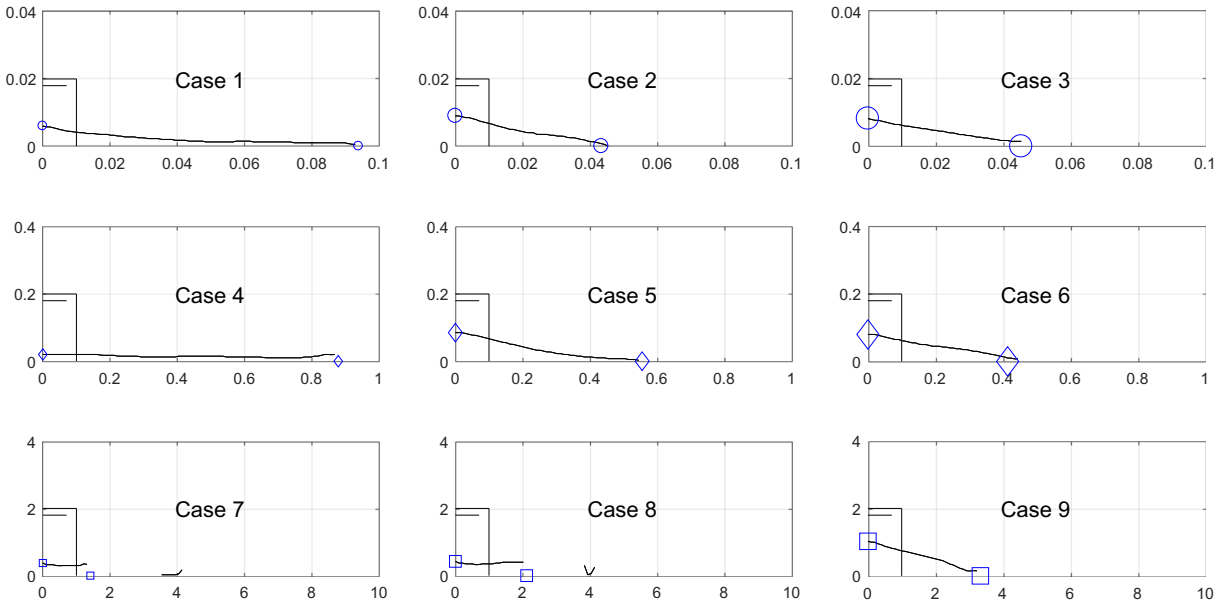

Fig. A.9. Time evolution of dimensional shapes (x and y positions of the cliff boundary) of sand in water for initial solid volume fraction $\alpha_{s,0} = 0.55$ and aspect ratio $a = 2$. For further description see caption of Fig. A.8.

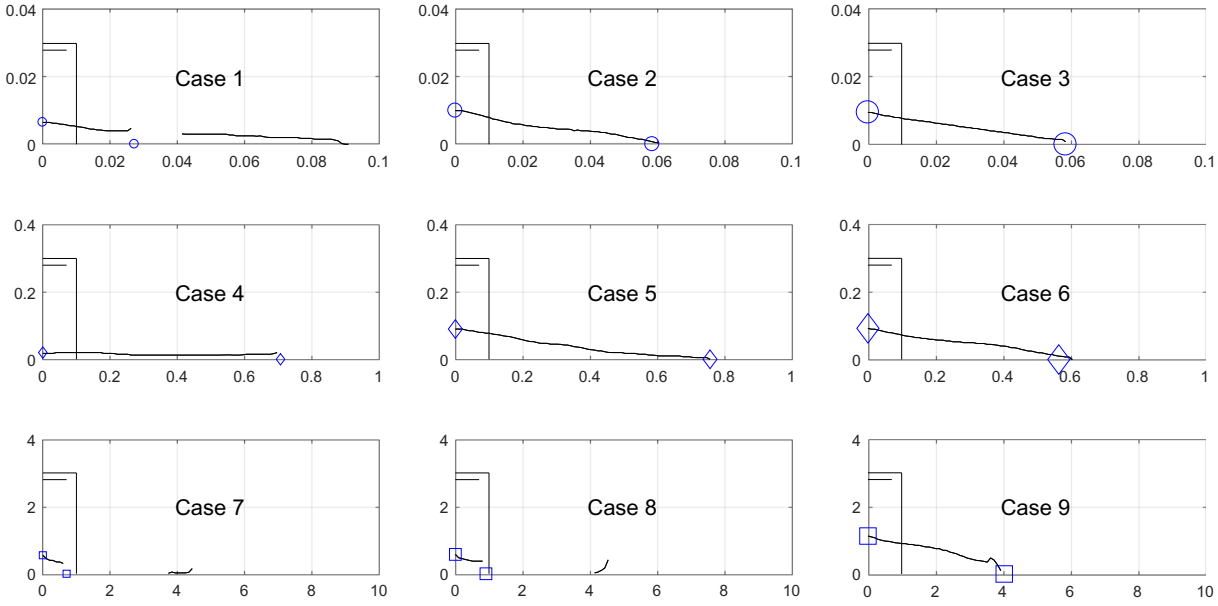

Fig. A.10. Time evolution of dimensional shapes (x and y positions of the cliff boundary) of sand in water for initial solid volume fraction $\alpha_{s,0} = 0.55$ and aspect ratio $a = 3$. For further description see caption of Fig. A.8.

A.3. . Initial solid volume fraction $\alpha_{s,0} = 0.60$

A.3.1. Air

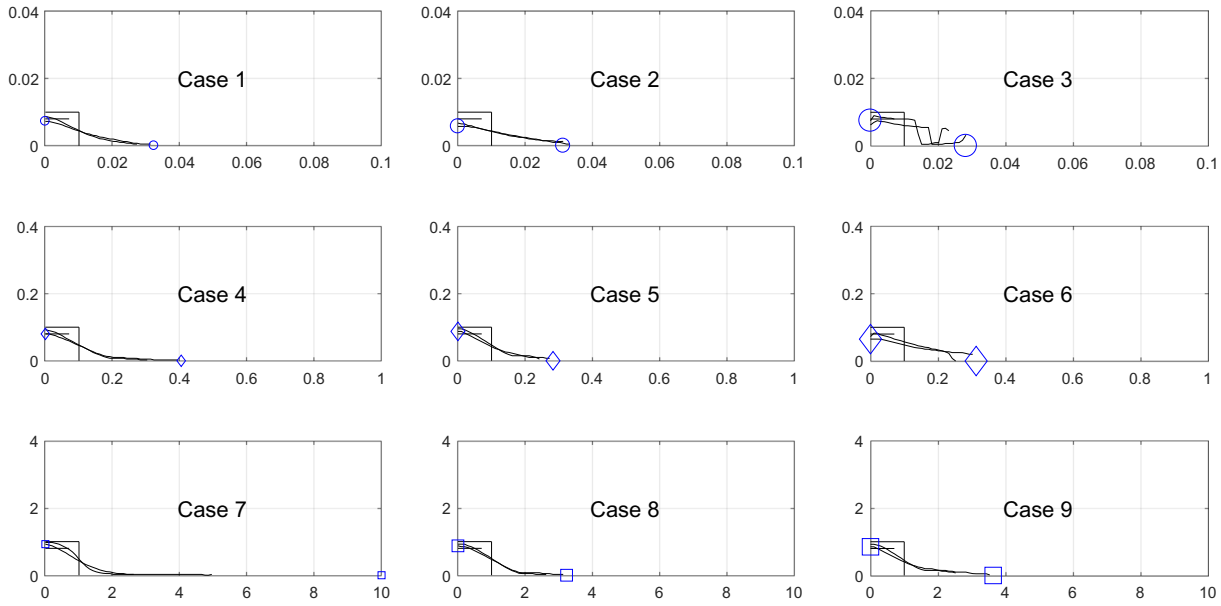

Fig. A.11. Time evolution of dimensional shapes (x and y positions of the cliff boundary) of sand in air for initial solid volume fraction $\alpha_{s,0} = 0.60$ and aspect ratio $a = 1$ and the different cases as given by Table 3. The individual shapes represent the collapsing cliff at $t = 0, 2$ s. The final values of $x_f = x(t = 2\ \text{s})$ and $y_f = y(t = 2\ \text{s})$ *are highlighted and correspond to the values depicted in* Fig. 7.

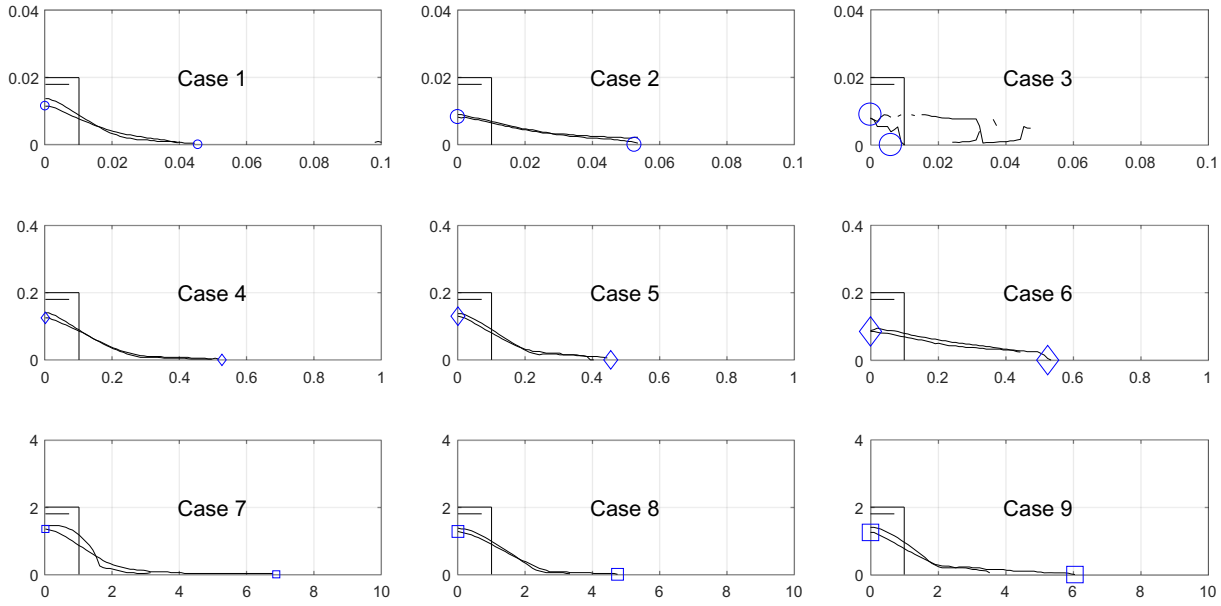

Fig. A.12. Time evolution of dimensional shapes (x and y positions of the cliff boundary) of sand in air for initial solid volume fraction $\alpha_{s,0} = 0.60$ and aspect ratio $a = 2$. For further description see caption of Fig. A.11.

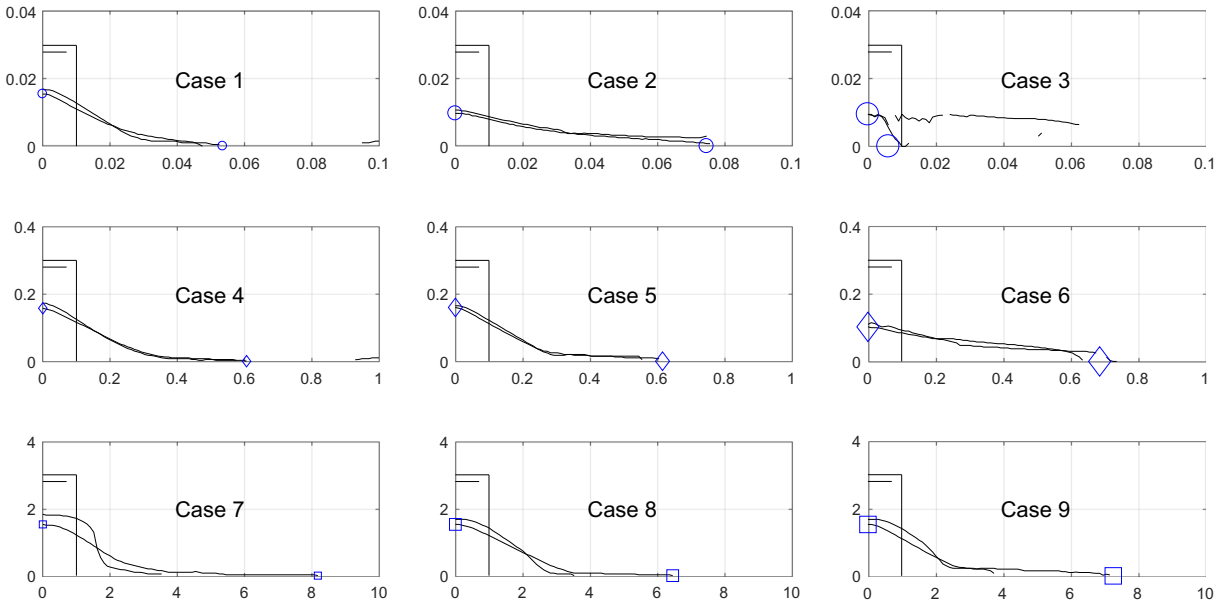

Fig. A.13. Time evolution of dimensional shapes (x and y positions of the cliff boundary) of sand in air for initial solid volume fraction $\alpha_{s,0} = 0.60$ and aspect ratio $a = 3$. For further description see caption of Fig. A.11.

A.3.2. H2O

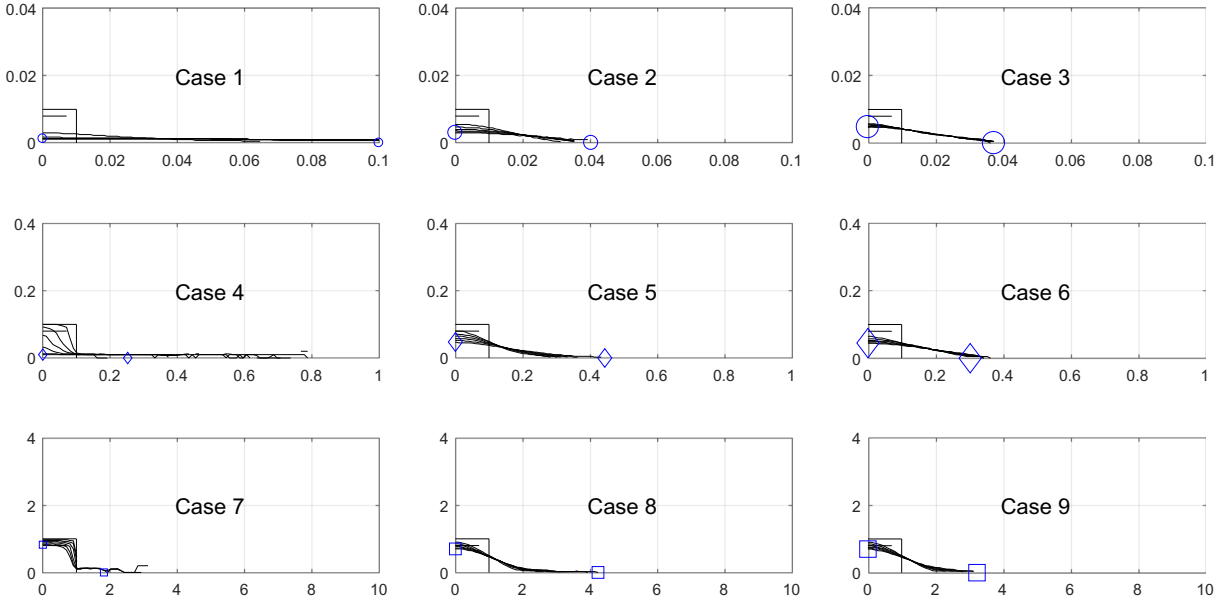

Fig. A.14. Time evolution of dimensional shapes (x and y positions of the cliff boundary) of sand in water for initial solid volume fraction $\alpha_{s,0} = 0.60$ and aspect ratio $a = 1$ and the different cases as given by Table 3. The individual shapes represent the collapsing cliff at $t = 0, 10, 20, \ldots, 60$ s. The final values of $x_f = x(t = 60\,\text{s})$ and $x_f = y(t = 60\,s)$ *are highlighted and correspond to the values depicted in* Fig. 10.

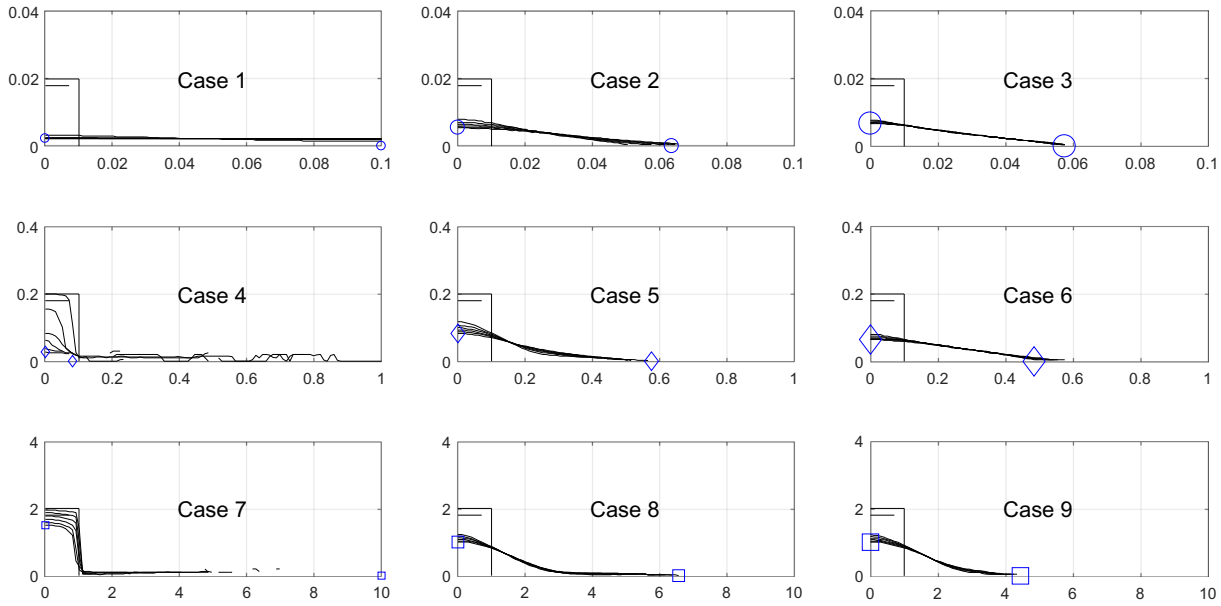

Fig. A.15. Time evolution of dimensional shapes (x and y positions of the cliff boundary) of sand in water for initial solid volume fraction $\alpha_{s,0} = 0.60$ and aspect ratio $a = 2$. For further description see caption of Figure Fig. A.14.

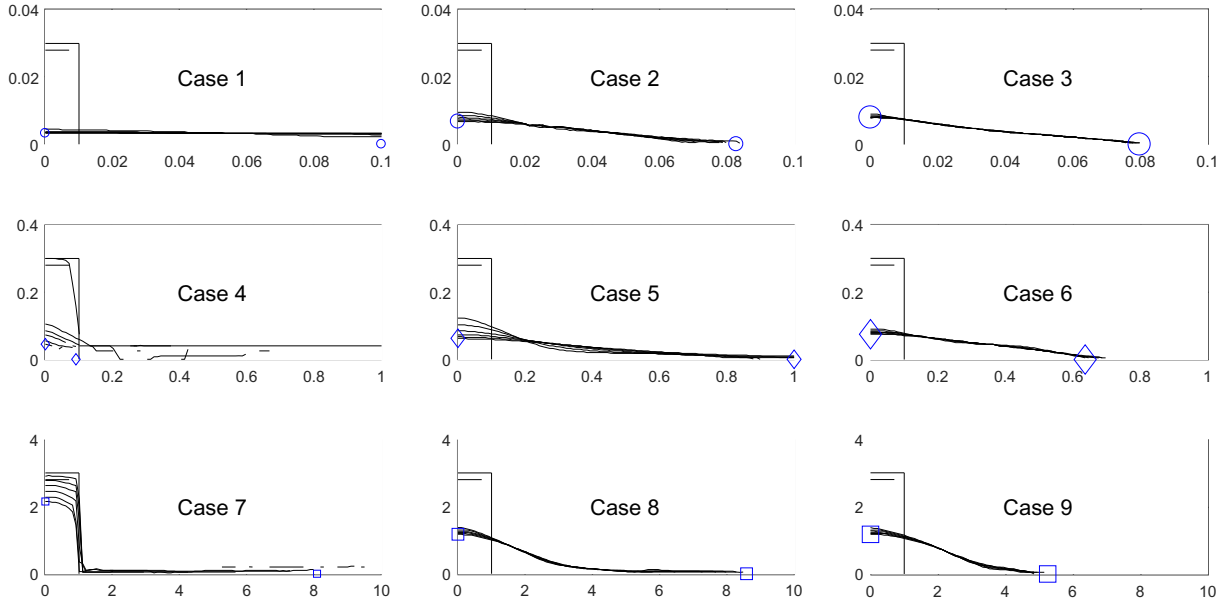

Fig. A.16. Time evolution of dimensional shapes (x and y positions of the cliff boundary) of sand in water for initial solid volume fraction $\alpha_{s,0} = 0.60$ and aspect ratio $a = 3$. For further description see caption of Fig. A.14.

Appendix B. Field plots for $\alpha_{s,0} \approx 0.59$, $a = 3$, air, #5

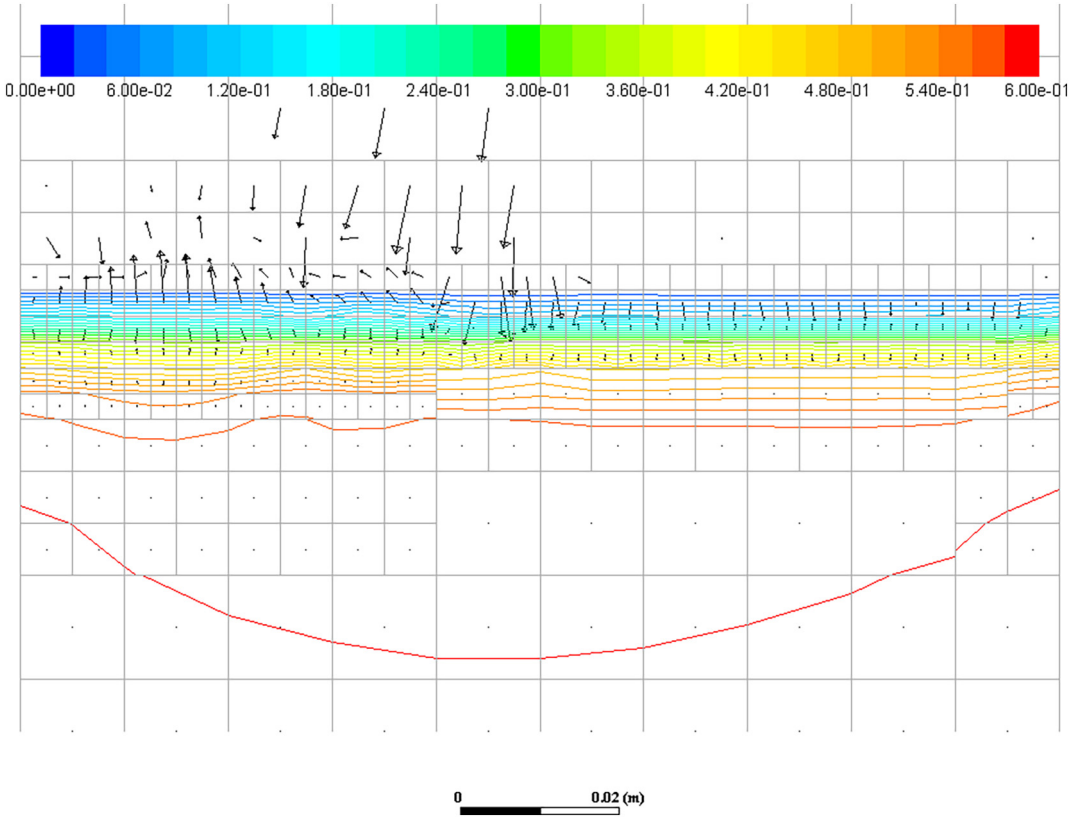

Fig. B.1. Solid volume fraction and solid velocity (result of $\alpha_{s,0} \approx 0.59$, $a = 3$, air, #5 pre-simulation, zoom on top of bed, maximum solid velocity 0.47 m/s).

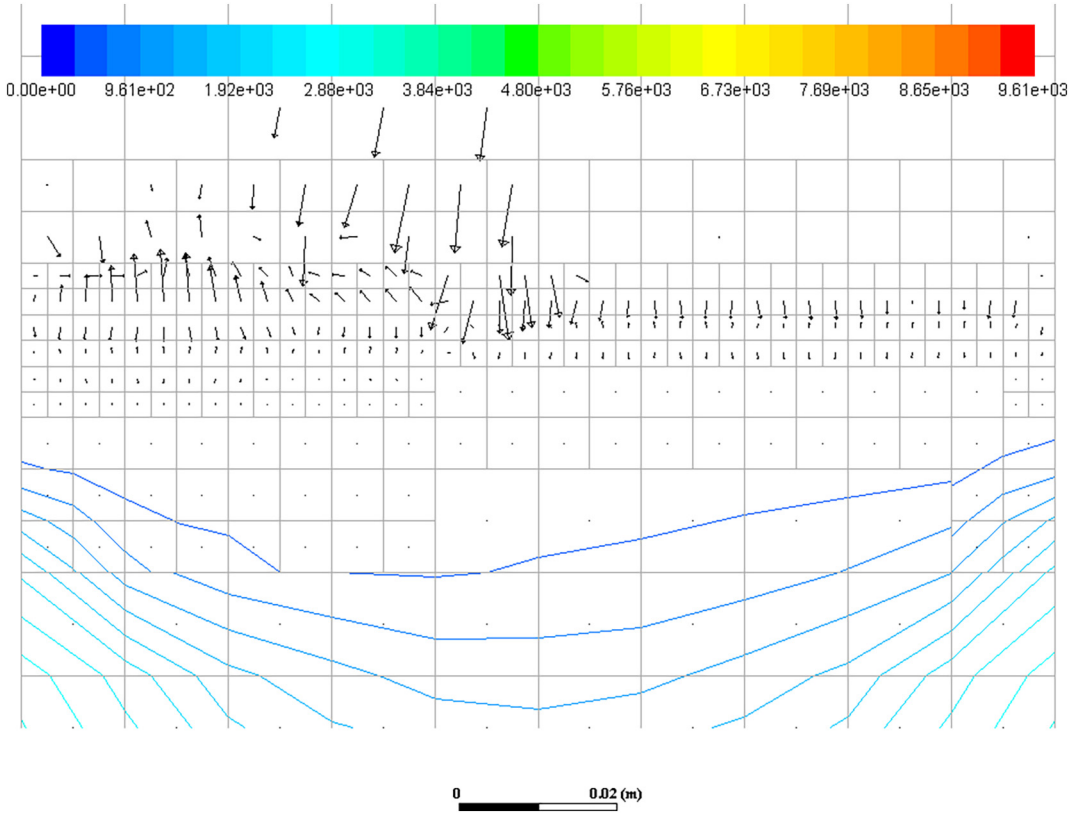

Fig. B.2. Solid pressure and solid velocity (result of $\alpha_{s,0} \approx 0.59$, $a = 3$, air, #5 pre-simulation, zoom on top of bed, maximum solid velocity 0.47 m/s).

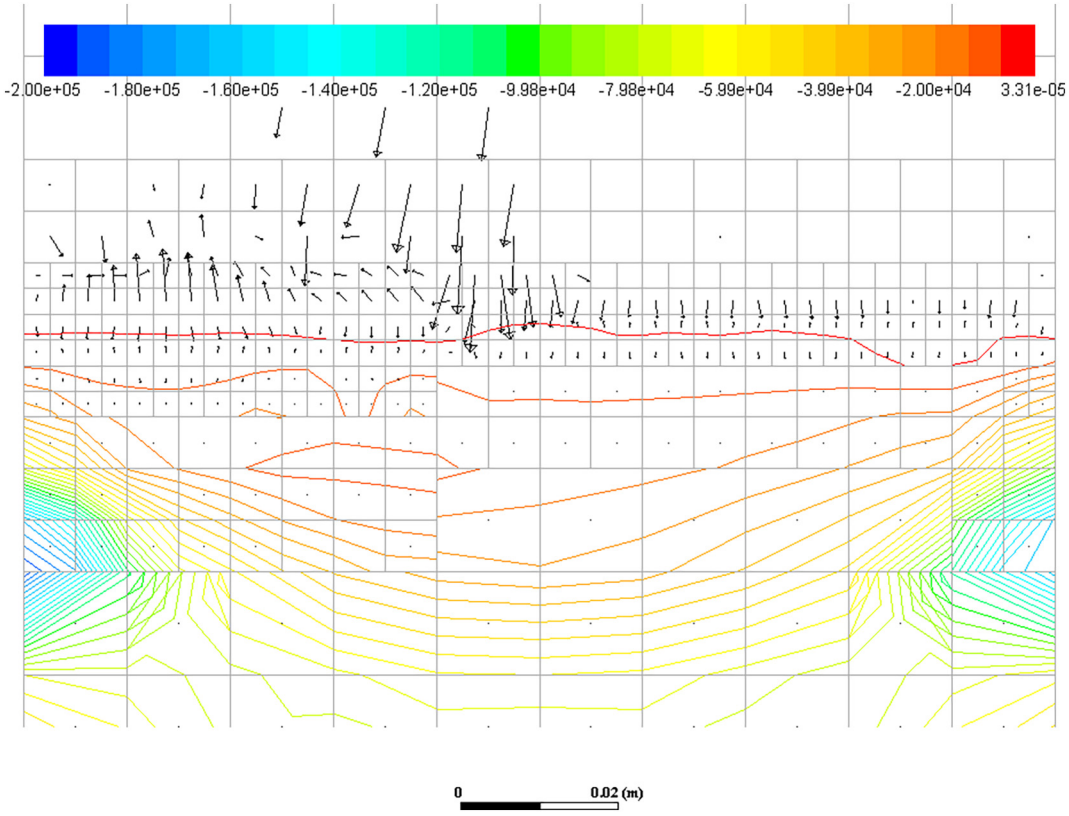

Fig. B.3. y-component of solid pressure gradient (result of $\alpha_{s,0} \approx 0.59$, $a = 3$, air, #5 pre-simulation, zoom on top of bed, maximum solid velocity 0.47 m/s).

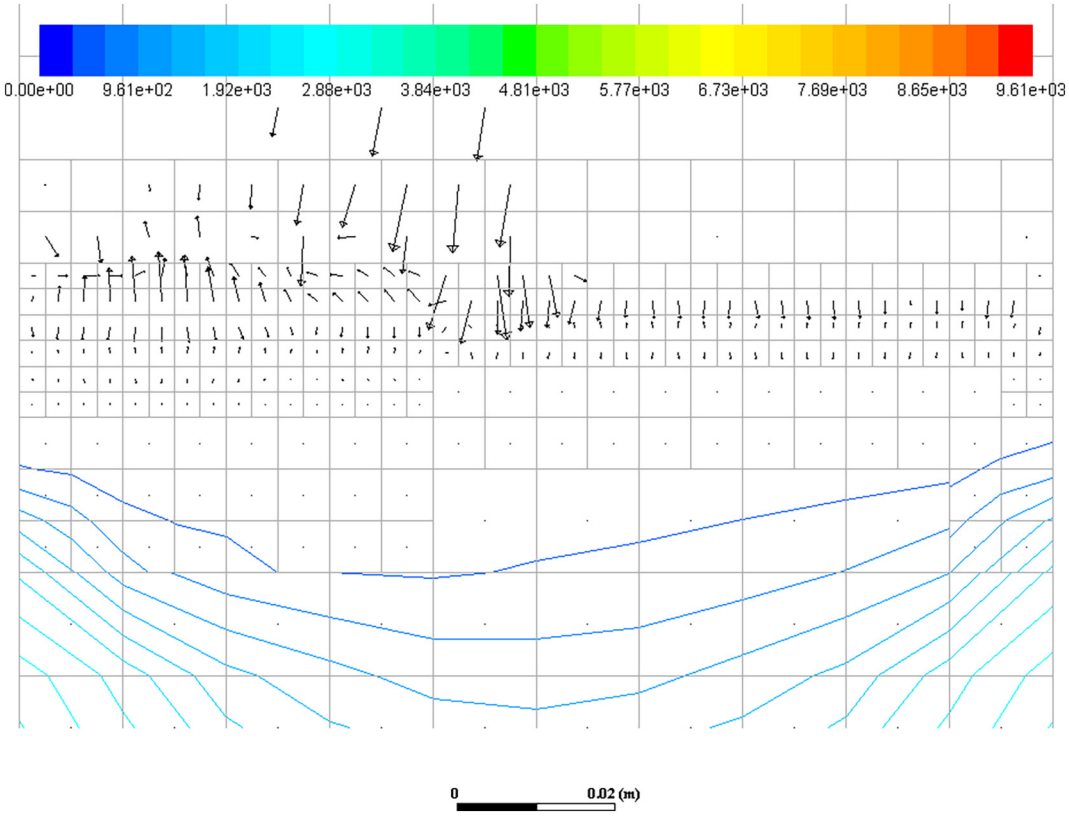

Fig. B.4. Frictional pressure and solid velocity (result of $\alpha_{s,0} \approx 0.59$, $a = 3$, air, #5 pre-simulation, zoom on top of bed, maximum solid velocity 0.47 m/s).

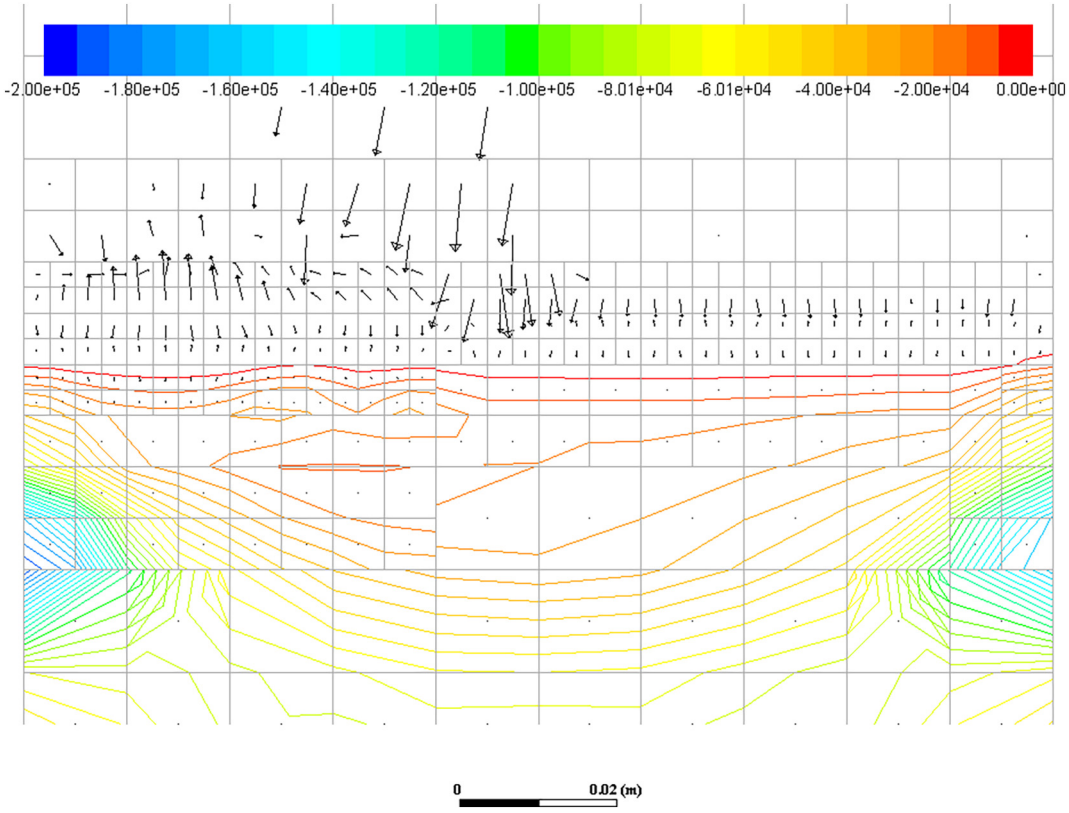

Fig. B.5. y-component of frictional pressure gradient (result of $\alpha_{s,0} \approx 0.59$, $a = 3$, air, #5 pre-simulation, zoom on top of bed, maximum solid velocity 0.47 m/s).

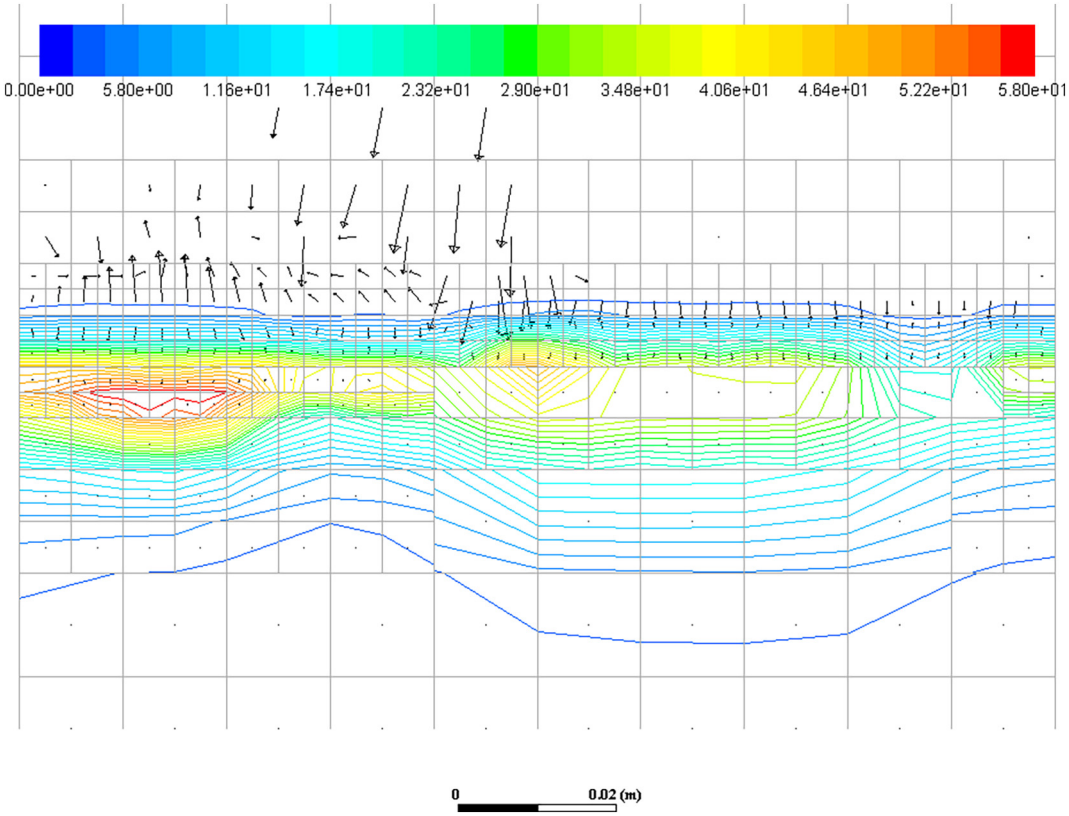

Fig. B.6. Kinetic/collisional pressure and solid velocity (result of $\alpha_{s,0} \approx 0.59$, $a = 3$, air, #5 pre-simulation, zoom on top of bed, maximum solid velocity 0.47 m/s).

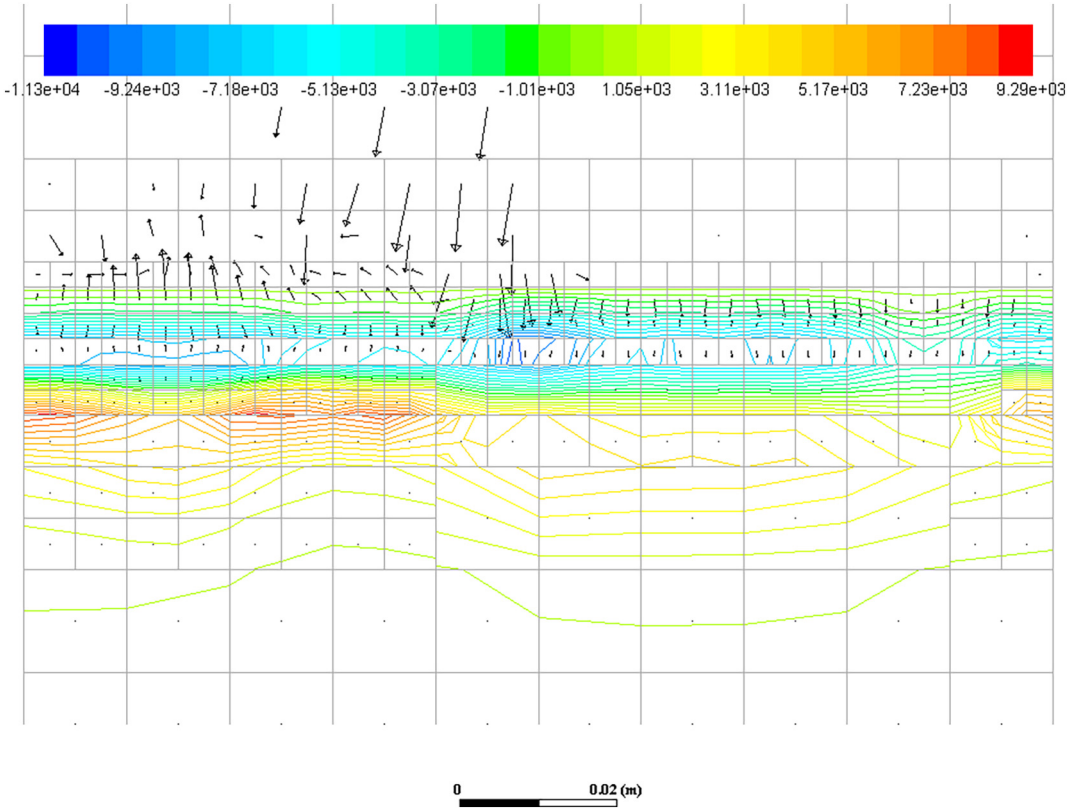

Fig. B.7. y-component of kinetic/collisional pressure gradient and solid velocity (result of $\alpha_{s,0} \approx 0.59$, $a = 3$, air, #5 pre-simulation, zoom on top of bed, maximum solid velocity 0.47 m/s).

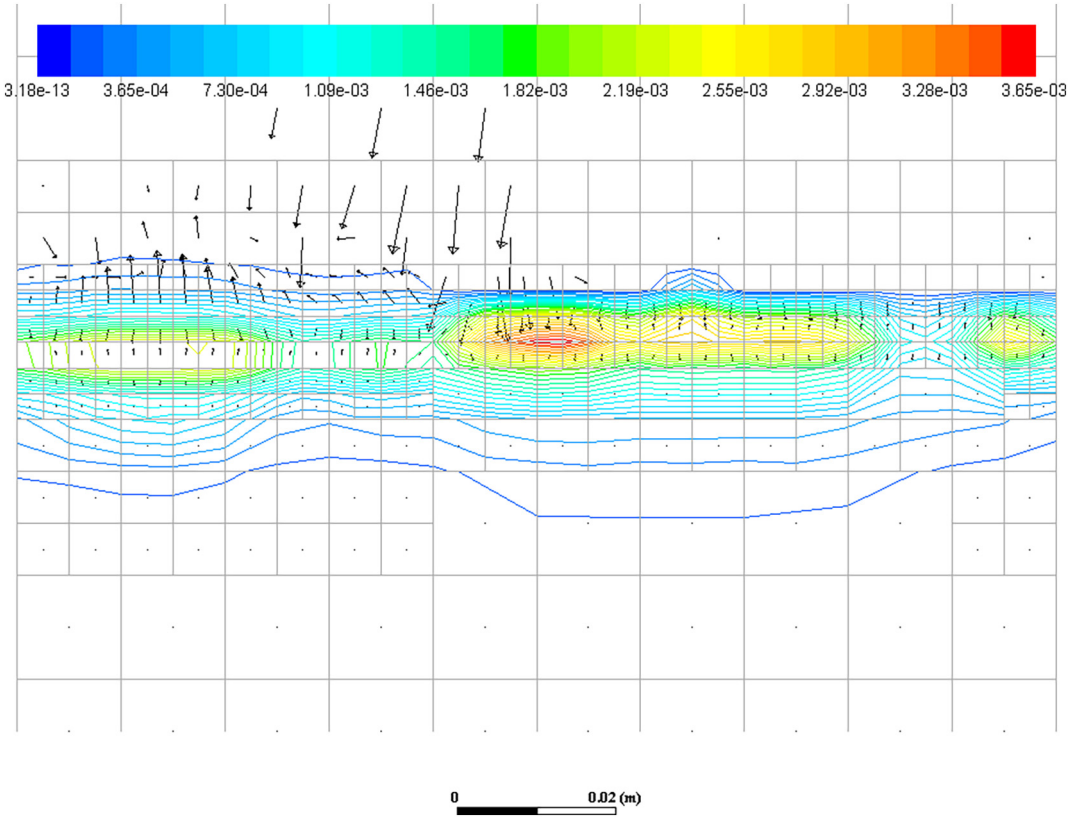

Fig. B.8. Granular temperature and solid velocity (result of $\alpha_{s,0} \approx 0.59$, $a = 3$, air, #5 pre-simulation, zoom on top of bed, maximum solid velocity 0.47 m/s).

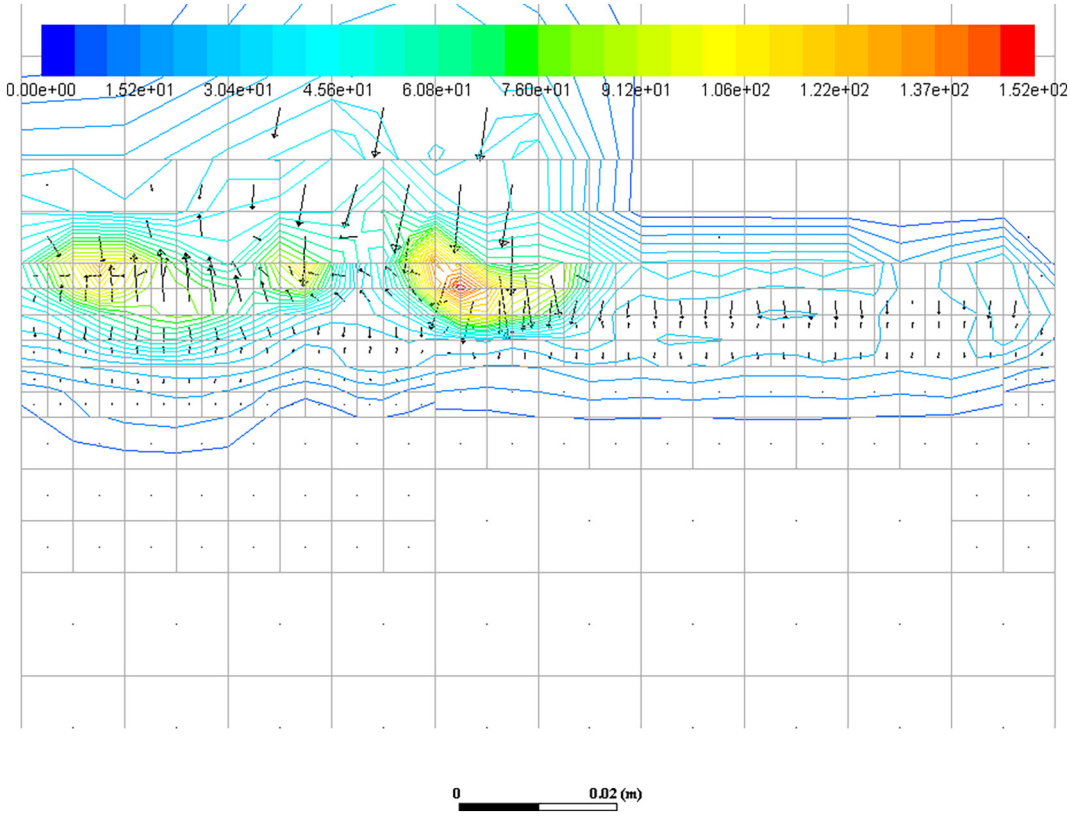

Fig. B.9. Solid strain rate and solid velocity (result of $\alpha_{s,0} \approx 0.59$, $a = 3$, air, #5 pre-simulation, zoom on top of bed, maximum solid velocity 0.47 m/s).

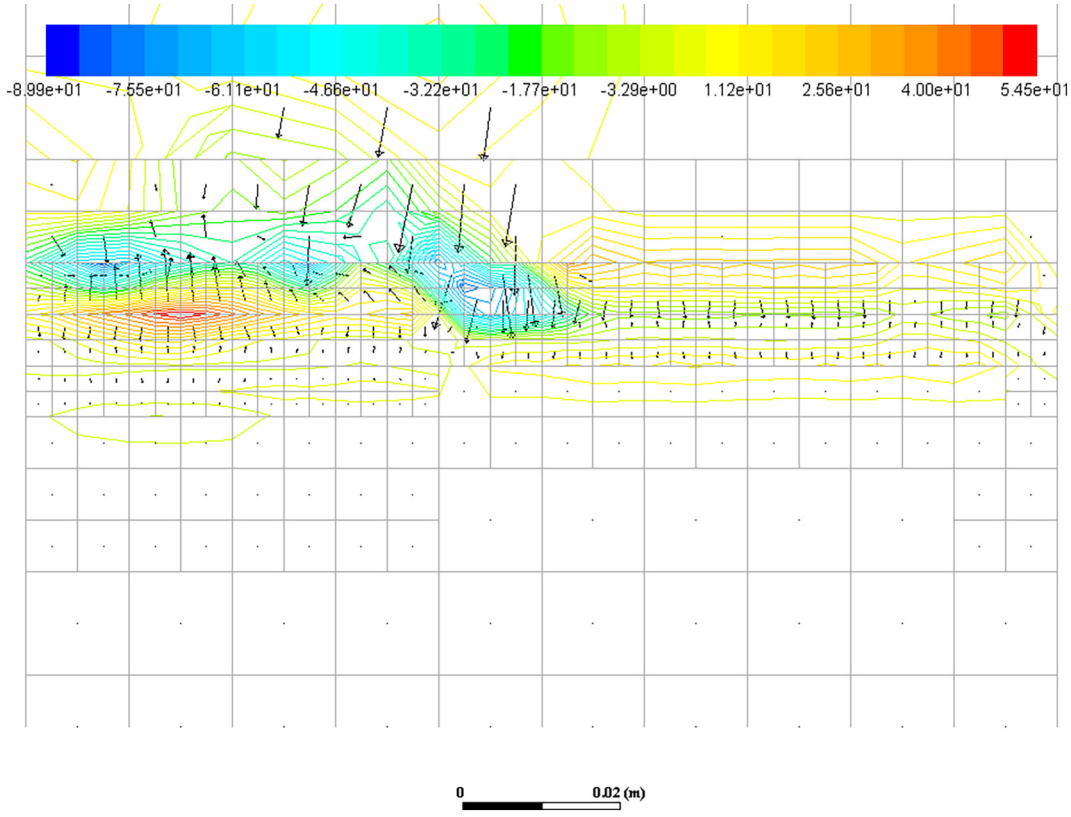

Fig. B.10. Solid $\partial u/\partial y$ and solid velocity (result of $\alpha_{s,0} \approx 0.59$, $a = 3$, air, #5 pre-simulation, zoom on top of bed, maximum solid velocity 0.47 m/s).

References

[1] R. Delannay, A. Valance, A. Mangeney, O. Roche, P. Richard, Granular and particle-laden flows: from laboratory experiments to field observations, J. Phys. D. Appl. Phys. 50 (5) (Feb. 2017), 053001.
[2] A. Bougouin, L. Lacaze, Granular collapse in a fluid: different flow regimes for an initially dense-packing, Physical Review Fluids 3 (6) (Jun. 2018).
[3] G. Lube, H.E. Huppert, R.S.J. Sparks, A. Freundt, Collapses of two-dimensional granular columns, Phys. Rev. E 72 (4) (Oct. 2005).
[4] A. Mangeney, O. Roche, O. Hungr, N. Mangold, G. Faccanoni, A. Lucas, Erosion and mobility in granular collapse over sloping beds, J. Geophys. Res. 115 (F3) (Sep. 2010).
[5] S.J. de Vet, B. Yohannes, K.M. Hill, J.R. de Bruyn, Collapse of a rectangular well in a quasi-two-dimensional granular bed, Phys. Rev. E 82 (4) (Oct. 2010).
[6] S.J. de Vet, J.R. de Bruyn, Shape of impact craters in granular media, Phys. Rev. E 76 (4) (Oct. 2007).
[7] S. Siavoshi, A. Kudrolli, Failure of a granular step, Phys. Rev. E 71 (5) (May 2005).
[8] E.L. Thompson, H.E. Huppert, Granular column collapses: further experimental results, J. Fluid Mech. 575 (Mar. 2007) 177.
[9] L. Lacaze, J.C. Phillips, R.R. Kerswell, Planar collapse of a granular column: experiments and discrete element simulations, Phys. Fluids 20 (6) (Jun. 2008), 063302.
[10] L. Rondon, O. Pouliquen, P. Aussillous, Granular collapse in a fluid: role of the initial volume fraction, Phys. Fluids 23 (7) (Jul. 2011), 073301.
[11] M. Pailha, et al., Initiation of Submarine Granular Avalanches: Role of the Initial Volume Fraction, 1027, 2008 935–937.
[12] P. Jop, Rheological properties of dense granular flows, Comptes Rendus Physique 16 (1) (Jan. 2015) 62–72.
[13] P. Jop, Y. Forterre, O. Pouliquen, A constitutive law for dense granular flows, Nature 441 (7094) (Jun. 2006) 727–730.
[14] F. da Cruz, S. Emam, M. Prochnow, J.-N. Roux, F. Chevoir, Rheophysics of dense granular materials: discrete simulation of plane shear flows, Phys. Rev. E 72 (2) (Aug. 2005).
[15] P.-Y. Lagrée, L. Staron, S. Popinet, The granular column collapse as a continuum: validity of a two-dimensional Navier–stokes model with a μ(I)-rheology, J. Fluid Mech. 686 (Nov. 2011) 378–408.
[16] T. Barker, D.G. Schaeffer, M. Shearer, J.M.N.T. Gray, Well-posed continuum equations for granular flow with compressibility and $\mu(I)$-rheology, Proc. R. Soc. A 473 (2201) (May 2017), 20160846.
[17] S.B. Savage, Granular flows down rough inclines - review and extension, Studies in Applied Mechanics, vol. 7, Elsevier 1983, pp. 261–282.
[18] S.B. Savage, R. Pfeffer, Z.M. Zhao, Solids transport, separation and classification, Powder Technol. 88 (3) (1996) 323–333.
[19] S.B. Savage, D.J. Jeffrey, The stress tensor in a granular flow at high shear rates, J. Fluid Mech. 110 (1981) 255–272.
[20] C.K.K. Lun, S.B. Savage, D.J. Jeffrey, N. Chepurniy, Kinetic theories for granular flow: inelastic particles in Couette flow and slightly inelastic particles in a general flowfield, J. Fluid Mech. 140 (1984) 223–256.
[21] P.C. Johnson, R. Jackson, Frictional–collisional constitutive relations for granular materials, with application to plane shearing, J. Fluid Mech. 176 (1987) 67–93.
[22] M. Syamlal, W. Rogers, T.J. O'Brien, *MFIX Documentation Theory Guide*. Morgantown: U.S. Department of Energy, Office of Fossil Energy, 1993.
[23] D.G. Schaeffer, Instability in the evolution equations describing incompressible granular flow, Journal of differential equations 66 (1) (1987) 19–50.
[24] S. Schneiderbauer, A. Aigner, S. Pirker, A comprehensive frictional-kinetic model for gas–particle flows: analysis of fluidized and moving bed regimes, Chem. Eng. Sci. 80 (Oct. 2012) 279–292.
[25] S. Chialvo, S. Sundaresan, A modified kinetic theory for frictional granular flows in dense and dilute regimes, Phys. Fluids 25 (7) (2013), 070603.
[26] K. Kumar, J.-Y. Delenne, K. Soga, Mechanics of granular column collapse in fluid at varying slope angles, Journal of Hydrodynamics, Ser. B 29 (4) (Aug. 2017) 529–541.
[27] C. Wang, Y. Wang, C. Peng, X. Meng, Two-fluid smoothed particle hydrodynamics simulation of submerged granular column collapse, Mech. Res. Commun. 79 (Jan. 2017) 15–23.
[28] H. Laux, "Modeling of Dilute and Dense Dispersed Fluid-Particle Two-Phase Flow," PhD Dissertation, Norwegian University of Science and Technology, Norway, Trondheim, 1998.
[29] I.R. Ionescu, A. Mangeney, F. Bouchut, O. Roche, Viscoplastic modeling of granular column collapse with pressure-dependent rheology, J. Non-Newtonian Fluid Mech. 219 (May 2015) 1–18.
[30] B.H. Ng, Y. Ding, M. Ghadiri, Assessment of the kinetic–frictional model for dense granular flow, Particuology 6 (1) (Feb. 2008) 50–58.
[31] S.B. Savage, M.H. Babaei, T. Dabros, Modeling gravitational collapse of rectangular granular piles in air and water, Mech. Res. Commun. 56 (Mar. 2014) 1–10.
[32] A. Nikolopoulos, N. Nikolopoulos, N. Varveris, S. Karellas, P. Grammelis, E. Kakaras, Investigation of proper modeling of very dense granular flows in the recirculation system of CFBs, Particuology 10 (6) (Dec. 2012) 699–709.
[33] E. Ghadirian, H. Arastoopour, Numerical analysis of frictional behavior of dense gas–solid systems, Particuology 32 (Jun. 2017) 178–190.
[34] D. Gidaspow, R. Bezburuah, J. Ding, Hydrodynamics of circulating fluidized beds: kinetic theory approach, *Fluidization VII, Proceedings of the 7th Engineering Foundation Conference on Fluidization*, Gold Coast, 1992.
[35] C.Y. Wen, Y.H. Yu, "Mechanics of fluidization," presented at the Chem. Eng. Prog., Symp. Ser, 62, 1966 100–111.
[36] S. Ergun, Fluid flow through packed columns, Chem. Eng. Prog. 48 (1952) 89–94.
[37] M.M. Cross, Rheology of non-Newtonian fluids: a new flow equation for pseudoplastic systems, J. Colloid Sci. 20 (5) (1965) 417–437.
[38] A. Busch, V. Myrseth, M. Khatibi, P. Skjetne, S. Hovda, S.T. Johansen, Rheological characterization of Polyanionic cellulose solutions with application to drilling fluids and cuttings transport modeling, Appl. Rheol. 28 (2) (2018) 1–16.
[39] J. Ding, D. Gidaspow, A bubbling fluidization model using kinetic theory of granular flow, AICHE J. 36 (4) (Apr. 1990) 523–538.
[40] R.A. Bagnold, Experiments on a gravity-free dispersion of large solid spheres in a Newtonian fluid under shear, Proceedings of the Royal Society of London. Series A. Mathematical and Physical Sciences 225 (1160) (1954) 49–63.
[41] S. Ogawa, A. Umemura, N. Oshima, On the equations of fully fluidized granular materials, Zeitschrift für angewandte Mathematik und Physik ZAMP 31 (4) (Jul. 1980) 483–493.
[42] J.L. Sinclair, R. Jackson, Gas-particle flow in a vertical pipe with particle-particle interactions, AICHE J. 35 (9) (Sep. 1989) 1473–1486.
[43] S. Vasquez, A phase coupled method for solving multiphase problems on unstructured mesh, Presented at the ASME 200 Fluids Engineering Division Summer Meeting, 2000.
[44] B.P. Leonard, A stable and accurate convective modelling procedure based on quadratic upstream interpolation, Comput. Methods Appl. Mech. Eng. 19 (1) (1979) 59–98.
[45] Inc ANSYS, ANSYS Fluent User Guide R17, vol. 2, ANSYS, Inc., Canonsburg, PA, 2016.
[46] Inc ANSYS, ANSYS Fluent Theory Guide R17, vol. 2, ANSYS, Inc., Canonsburg, PA, 2016.
[47] C.M. Rhie, W.L. Chow, Numerical study of the turbulent flow past an airfoil with trailing edge separation, AIAA J. 21 (11) (Nov. 1983) 1525–1532.
[48] H. Karema, Numerical treatment of inter-phase coupling and phasic pressures in multi-fluid modelling, VTT PUBLICATIONS 4 (5) (2002) 8.
[49] M. Syamlal, MFIX Documentation Numerical Technique. Morgantown, U.S. Department of Energy, Office of Fossil Energy, 1998.
[50] E.A. Meese, S.T. Johansen, A simulation concept for generic simulation of multi-material flow using staggered cartesian grids, *Progress in Applied CFD–CFD2017 Selected papers from 12th International Conference on Computational Fluid Dynamics in the Oil & Gas, Metallurgical and Process Industries*, Trondheim 2017, pp. 253–263.
[51] A. Passalacqua, R.O. Fox, Implementation of an iterative solution procedure for multi-fluid gas–particle flow models on unstructured grids, Powder Technol. 213 (1–3) (Nov. 2011) 174–187.
[52] C.M. Venier, S. Marquez Damian, N.M. Nigro, Numerical aspects of Eulerian gas–particles flow formulations, Comput. Fluids 133 (Jul. 2016) 151–169.
[53] S. Noelle, N. Pankratz, G. Puppo, J.R. Natvig, Well-balanced finite volume schemes of arbitrary order of accuracy for shallow water flows, J. Comput. Phys. 213 (2) (2006) 474–499.